Weakly nonlinear analysis of the viscoelastic instability in channel flow for finite and vanishing Reynolds numbers

Gergely Buza[1]† **Jacob Page**[2]‡ **and Rich R. Kerswell**[1]¶

[1]Department of Applied Mathematics and Theoretical Physics, University of Cambridge, CB3 0WA, UK.
[2]School of Mathematics, University of Edinburgh, EH9 3FD, UK

(Received ?; revised ?; accepted ?.)

The recently-discovered centre-mode instability of rectilinear viscoelastic shear flow (Garg et al. *Phy. Rev. Lett.* **121**, 024502, 2018) has offered an explanation for the origin of elasto-inertial turbulence (EIT) which occurs at lower Weissenberg (Wi) numbers. In support of this, we show using weakly nonlinear analysis that the subcriticality found in Page et al. (*Phys. Rev. Lett.* **125**, 154501, 2020) is generic across the neutral curve with the instability only becoming supercritical at low Reynolds (Re) numbers and high Wi. We demonstrate that the instability can be viewed as purely elastic in origin even for $Re = O(10^3)$, rather than 'elasto-inertial', as the underlying shear does *not* feed the kinetic energy of the instability. It is also found that the introduction of a realistic maximum polymer extension length, L_{max}, in the FENE-P model moves the neutral curve closer to the inertialess $Re = 0$ limit at a fixed ratio of solvent-to-solution viscosities, β. In the dilute limit ($\beta \to 1$) with $L_{max} = O(100)$, the linear instability can brought down to more physically-relevant $Wi \gtrsim 110$ at $\beta = 0.98$, compared with the threshold $Wi = O(10^3)$ at $\beta = 0.994$ reported recently by Khalid et al. (*Phys. Rev. Lett.* **127**, 134502, 2021) for an Oldroyd-B fluid. Again the instability is subcritical implying that inertialess rectilinear viscoelastic shear flow is nonlinearly unstable - i.e. unstable to finite amplitude disturbances - for even lower Wi.

Key words: viscoelasticity, shear flow, instability

1. Introduction

Viscoelastic flows have been of interest ever since the observation 70 years ago that a substantial reduction in viscous drag on a wall of a pipe carrying turbulent flow is possible after adding only a few parts per millon of long-chain polymers (Toms 1948). Just as curiously, adding further polymer quickly saturates this effect when the so-called 'maximum drag reduction' regime (MDR) is entered (Virk 1970), with skin friction reduced by ∼80% relative to its Newtonian value. Efforts to explain this phenomenon have naturally focussed on understanding how low polymer concentrations moderate Newtonian turbulence (NT) (e.g. Lumley 1969; Tabor & de Gennes 1986; Procaccia *et al.* 2008; White & Mungal 2008). However, the discovery of a new form of viscoelastic turbulence - 'elasto-inertial' turbulence (EIT) - in 2013 (Samanta *et al.* 2013; Dubief *et al.* 2013; Sid *et al.* 2018) which exists at large Reynolds number $Re = O(10^3)$ and Weissenberg number $Wi = O(10)$ has provided a competing and even less well understood possibility. Provided Wi is large enough, EIT can exist at much lower Re than NT explaining what has been labelled

† gb643@cam.ac.uk
‡ jacob.page@ed.ac.uk
¶ r.r.kerswell@damtp.cam.ac.uk

in the past as 'early turbulence' (Jones & Maddock 1966; Goldstein *et al.* 1969; Hansen & Little 1974; Draad *et al.* 1998; Samanta *et al.* 2013; Choueiri *et al.* 2018; Chandra *et al.* 2018). At higher but fixed Re, it is also possible, as the polymer concentration is steadily increased from zero, to relaminarize NT before triggering EIT (Choueiri *et al.* 2018; Chandra *et al.* 2018). In DNS, increasing Wi from a state of EIT quenches the flow down to a simple travelling wave solution and presumably laminar flow if Wi is large enough (e.g. see figure 2 in Page *et al.* 2020; Dubief *et al.* 2020). At even higher Re, it is currently unclear whether the two types of turbulence merge or co-exist, and how MDR fits into the situation remains an outstanding issue (e.g. Xi & Graham 2010, 2012; Graham 2014; Samanta *et al.* 2013; Choueiri *et al.* 2018, 2021; Lopez *et al.* 2019).

Further questions also exist as to how EIT relates to another form of viscoelastic turbulence - 'elastic' turbulence (ET) - that was discovered a decade earlier (Groisman & Steinberg 2000). This is generated by the well-known 'elastic' linear instability of curved streamlines (Larson *et al.* 1990; Shaqfeh 1996) and exists at vanishingly small Reynolds numbers so inertial effects are unambiguously irrelevant for sustaining the turbulence. This elastic instability is also possible in planar geometries, but requires finite-amplitude disturbances to generate streamline curvature (Meulenbroek *et al.* 2004; Morozov & Saarloos 2007). Intriguingly, substantial linear transient growth can occur in the purely-elastic limit via a polymeric 'lift-up' effect, with streaks in the streamwise velocity (Jovanović & Kumar 2010, 2011), but is very different in appearance to these finite-amplitude solutions. In contrast to the inertialess ET, a fairly large Re is required for EIT, indicating that inertia is important here. This suggests that EIT and ET are distinct phenomena (e.g. see figure 30 Chaudhary *et al.* 2021) yet they could still be two extremes of the same whole (Samanta *et al.* 2013; Qin *et al.* 2019; Choueiri *et al.* 2021; Steinberg 2021). Finally, the underlying mechanism which sustains EIT has yet to be clarified (Dubief *et al.* 2013; Terrapon *et al.* 2015; Sid *et al.* 2018; Shekar *et al.* 2018, 2020; Page *et al.* 2020; Chaudhary *et al.* 2021).

A major step forward in explaining the origin of EIT was made recently when a linear instability was found at relatively high $Wi \gtrsim 20$ which could reach down to a threshold $Re_c \approx 63$ in pipe flow (Garg *et al.* 2018; Chaudhary *et al.* 2021). This finding overturned a long held view that no new linear instability would appear by adding polymers to a Newtonian rectilinear shear flow: see Chaudhary *et al.* (2019, 2021) for an extensive historical discussion of this point and the recent review by Sanchez *et al.* (2022). This instability was also confirmed in channel flow (Khalid *et al.* 2021*a*) using an Oldroyd-B fluid but was found absent in an upper-convected Maxwell (UCM) fluid (Chaudhary *et al.* 2019). The instability is a centre-mode instability which has a phase speed close to the maximum base-flow speed and appeared to need inertia (finite Re) to exist: in a channel with an experimentally-relevant β (the ratio of solvent-to-solution viscosities) of 0.9 and elasticity number of 0.1, the threshold $Re_c \approx 200$ (Khalid *et al.* 2021*a*) consistent with the finite threshold of $Re_c \approx 63$ found earlier in pipe flow (Garg *et al.* 2018; Chaudhary *et al.* 2021). However, in the dilute limit ($\beta \to 1$) and in contrast with pipe flow, Khalid *et al.* (2021*a*) alsofound that Re_c could be pushed down to ≈ 5 by the time β reached 0.99, albeit at very large Wi (=O(10^3)). Further computations (Khalid *et al.* 2021*b*) have confirmed that the elastic limit of $Re = 0$ can indeed be reached at $\beta = 0.9905$ and $Wi \approx 2500$. Looking beyond the extreme value of Wi –which *is* apparently achievable experimentally (Vashney & Steinberg 2018; Schnapp & Steinberg 2021)–this result has established a fascinating connection between an instability which appears to need inertia, elasticity and solvent viscosity (finite $(1-\beta)$) and a purely elastic instability when $(1-\beta)$ is small enough (Khalid *et al.* (2021*b*) refer to this as an 'ultra dilute' polymer solution).

However, EIT appears at lower Wi (figure 2 in Page *et al.* 2020) and sometimes lower Re at a given Wi (see figure 1b in Choueiri *et al.* 2021) than the centre-mode instability. For example, in channel flow at $Re = 1000$ and $\beta = 0.9$ in a FENE-P fluid with $L_{max} = 500$, EIT occurs around $Wi = 20$, whereas the centre-mode instability threshold is $Wi \approx 70$ (figure 2 (left) in Page *et al.* 2020). This means that if EIT is dynamically connected to this instability, the hierarchy

of nonlinear solutions which emerge from the linear instability must be substantially subcritical, reaching to Wi far below those of the neutral curve (and similarly for Re for high enough Wi). This was confirmed in one specific case on the neutral curve - $(Re, Wi, \beta) = (60, 26.9, 0.9)$ – where the bifurcation was shown to be strongly subcritical with the branch of travelling waves solutions reaching down to $Wi = 8.77$ (Page *et al.* 2020). Moreover, the travelling wave solutions adopt a distinctive 'arrowhead' form in the polymer stress when Wi is small enough which can be recognised as an intermittently-observed coherent structure in the DNS of EIT (Dubief *et al.* 2020).

The primary purpose of this paper is to back up this initial finding of subcriticality by carrying out a systematic survey of whether the centre mode bifurcation is sub- or supercritical across the entire neutral curve for a typical value of β of 0.9 using weakly nonlinear analysis (Stuart 1960; Watson 1960). In doing so, we also take the opportunity to confirm that the instability is present for a FENE-P fluid with reasonable maximum polymer extension L_{max} (see 2.1*d*) and, spurred on by the recent results of Khalid *et al.* (2021*b*), explore how the presence of finite L_{max} affects the dilute limit ($\beta \to 1$) where $Re = 0$ can be reached. We also examine the energetic source term, or terms, for the instability uncovering a consistent picture even on the part of the neutral curve reaching to high Re.

The plan of the paper is as follows. In §2, the FENE-P model is introduced and the presence or not of polymer diffusion as indicated by a Schmidt number Sc is discussed. The weakly nonlinear expansions are also introduced. While this is now an established method in the fluid dynamicists' toolbox, for viscoelastic models where the (coarse-grained) local polymer configuration is represented by a positive definite conformation tensor $\mathbf{C}$, there are some technicalities which need some attention. We follow the framework recently suggested by Hameduddin *et al.* (2018, 2019) to treat this issue which requires a bit more formal development than is normal. Having set this up, §3 then presents the weakly nonlinear analysis which proceeds as usual albeit with a proxy for $\mathbf{C}$ being expanded instead of $\mathbf{C}$ itself. Results in §4 are arranged as follows: §4.1 and §4.2 consider $(\beta, L_{max}) = (0.9, 500)$ with $Sc \to \infty$; §4.3 considers $(\beta, L_{max}, Sc) = (0.9, 100, 10^6)$; §4.4 performs an energy analysis over the neutral curves of §4.1 and 4.3; and finally §4.5 examines the $Re = 0$ situation varying β over the approximate range of $[0.97, 0.99]$ for $Wi \leqslant 200$ and $L_{max} \in [40, 100]$ ($Sc \to \infty$). More moderate β are considered in Appendix C, specifically $(\beta, L_{max}) = (0.74, \{250, 500, \infty\})$ and $(0.56, \{500, \infty\})$ (all at $Sc \to \infty$). Lastly, §5 presents a discussion of the paper's results.

While this work was going through review, we became aware of the complementary work of Wan *et al.* (2021) on the weakly nonlinear analysis of axisymmetric pipe flow. Their findings are consistent with those reported here for channel flow.

2. Formulation

We consider pressure-driven viscoelastic flow between two parallel, stationary, rigid plates separated by a distance $2h$ and assume that the flow is governed by the FENE-P model

$$\partial_t \mathbf{u} + (\mathbf{u} \cdot \boldsymbol{\nabla})\,\mathbf{u} + \boldsymbol{\nabla} p = \frac{\beta}{Re}\Delta\mathbf{u} + \frac{(1-\beta)}{Re}\boldsymbol{\nabla} \cdot \mathbf{T}(\mathbf{C}), \tag{2.1a}$$

$$\boldsymbol{\nabla} \cdot \mathbf{u} = 0, \tag{2.1b}$$

$$\partial_t \mathbf{C} + (\mathbf{u} \cdot \boldsymbol{\nabla})\,\mathbf{C} + \mathbf{T}(\mathbf{C}) = \mathbf{C} \cdot \boldsymbol{\nabla}\mathbf{u} + (\boldsymbol{\nabla}\mathbf{u})^T \cdot \mathbf{C} + \frac{1}{ReSc}\Delta\mathbf{C}. \tag{2.1c}$$

The constitutive relation for the polymer stress, $\mathbf{T}$, is given by the Peterlin function

$$\mathbf{T}(\mathbf{C}) := \frac{1}{Wi}\Big(f(\mathrm{tr}\,\mathbf{C})\mathbf{C} - \mathbf{I}\Big), \quad \text{where} \quad f(x) := \left(1 - \frac{x-3}{L_{max}^2}\right)^{-1} \tag{2.1d}$$

with L_{max} denoting the maximum extensibility of polymer chains. Here $\mathbf{C} \in \mathrm{Pos}(3)$ (the set of positive definite 3×3 matrices) is the polymer conformation tensor and $\beta \in [0, 1]$ denotes the viscosity ratio, $\beta := \nu_s/\nu$, where ν_s and $\nu_p = \nu - \nu_s$ are the solvent and polymer contributions to the total kinematic viscosity ν. The equations are non-dimensionalised by h and the bulk speed

$$U_b := \frac{1}{2h}\int_{-h}^{h} u_x \, dy \tag{2.2}$$

which, through adjusting the pressure gradient appropriately, is kept constant so that the Reynolds and Weissenberg numbers are defined as

$$Re := \frac{hU_b}{\nu}, \quad Wi := \frac{\tau U_b}{h} \tag{2.3}$$

where τ is the polymer relaxation time. Polymer diffusion - the last term in Eq. (2.1*c*) - is often omitted as the typical magnitude of the Schmidt number, $Sc \sim O(10^6)$. Here it is retained throughout the nonlinear analysis to: i) allow a more realistic comparison with results from direct numerical simulations (DNS), where a relatively low Schmidt number ($Sc \sim O(10^3)$) is required for the solver to converge (Page *et al.* 2020), and ii) assess its importance more generally. Non-slip boundary conditions are imposed on the velocity field. If an infinite Schmidt number Sc is considered, no boundary conditions for the conformation tensor $\mathbf{C}$ are needed. In the case of finite Schmidt numbers, we apply $Sc \to \infty$ at the boundary to retain this situation (Sid *et al.* 2018).

In the course of this work, we compute neutral curves for the recently-discovered centre mode instability (Garg *et al.* 2018) in a channel following the recent work by Khalid *et al.* (2021*a*,*b*). The marginally-stable eigenfunctions form the basis of a weakly nonlinear expansion in the amplitude of the bifurcating solution. The key objective here is to ascertain whether the bifurcation is supercritical or subcritical. Subcriticality would indicate that bifurcated solutions exist beyond the parameter domain of linear instability, thereby implying that the flow is nonlinearly unstable - i.e. unstable to sufficiently large amplitude disturbances - in new, potentially more interesting parameter regimes. A case in point is the very recent discovery that the centre mode instability still operates at $Re = 0$ albeit at very high $Wi = O(1000)$ and ultra-dilute polymer solutions of $1 - \beta = O(10^{-3})$ (Khalid *et al.* 2021*b*). While these extremes are on the margins of physical relevance, a strongly-subcritical instability could still see its consequences in the form of finite amplitude solutions at vastly different Wi and β.

2.1. *Base state*

The base state to (2.1*a*)-(2.1*c*) is the steady unidirectional solution and satisfies the following reduced set of equations:

$$\partial_x p = \frac{\beta}{Re}\partial_{yy}u_x + \frac{(1-\beta)}{ReWi}\left[\frac{(f(\mathrm{tr}\,\mathbf{C}))^2}{L_{max}^2}\mathrm{tr}(\partial_y C)C_{xy} + f(\mathrm{tr}\,\mathbf{C})\partial_y C_{xy}\right], \tag{2.4a}$$

$$\frac{1}{Wi}\left(f(\mathrm{tr}\,\mathbf{C})C_{xx} - 1\right) = 2C_{xy}\partial_y u_x + \frac{1}{ReSc}\partial_{yy}C_{xx}, \tag{2.4b}$$

$$\frac{1}{Wi}\left(f(\mathrm{tr}\,\mathbf{C})C_{yy} - 1\right) = \frac{1}{ReSc}\partial_{yy}C_{yy}, \tag{2.4c}$$

$$\frac{1}{Wi}\left(f(\mathrm{tr}\,\mathbf{C})C_{zz} - 1\right) = \frac{1}{ReSc}\partial_{yy}C_{zz}, \tag{2.4d}$$

$$\frac{1}{Wi}\left(f(\mathrm{tr}\,\mathbf{C})C_{xy}\right) = C_{yy}\partial_y u_x + \frac{1}{ReSc}\partial_{yy}C_{xy}. \tag{2.4e}$$

where $\mathbf{u} = u_x\hat{\mathbf{x}} + u_y\hat{\mathbf{y}}$. Since the Re is based on the bulk speed, the applied pressure gradient is adjusted until the bulk speed is unity (after non-dimensionalisation) (e.g. Samanta *et al.* 2013; Dubief *et al.* 2013; Sid *et al.* 2018; Dubief *et al.* 2020). Figure 1 displays the base state $(\mathbf{u}_b, p_b, \mathbf{C}_b)$

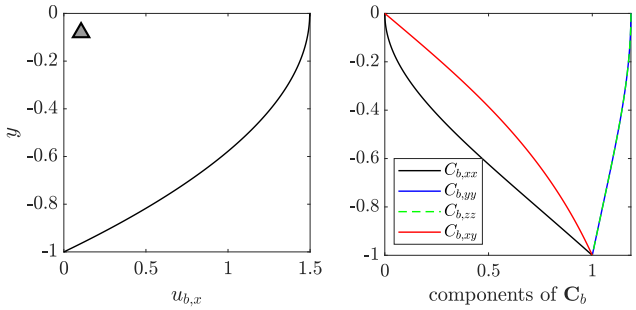

FIGURE 1. Laminar base state at $\beta = 0.9$, $L_{max} = 500$, $Sc \to \infty$, $Wi = 60$, $Re = 68$. The components of the base flow conformation tensor, $\mathbf{C}_b$, are normalized by their value at the bottom wall ($y = -1$). ($C_{b,xx}\big|_{y=-1} = 39235$, $C_{b,yy}\big|_{y=-1} = C_{b,zz}\big|_{y=-1} = 0.84$, $C_{b,xy}\big|_{y=-1} = 129$.)

for a particular parameter combination. It is worth remarking that U_{max} is very nearly 1.5 in units of U_b for β close to 1 (e.g. $\beta = 0.9$ which is used in the main part of the paper) and then a Wi based upon the bulk velocity (as here) is very close to two thirds of a Weissenberg number based on U_{max} (Garg *et al.* 2018; Chaudhary *et al.* 2021; Khalid *et al.* 2021*a*,*b*). In Appendix C we consider $\beta = 0.56$ and $\beta = 0.74$ where this simple relationship no longer holds.

2.2. *Perturbative Expansions*

The weakly nonlinear expansions for the velocity and pressure components are straightforwardly written in the form

$$\mathbf{u} = \mathbf{u}_b + \sum_{k=1}^{N} \varepsilon^k \mathbf{u}_{(k)}, \quad p = p_b + \sum_{k=1}^{N} \varepsilon^k p_{(k)}. \tag{2.5}$$

However, the conformation tensor, $\mathbf{C}$, calls for a more careful treatment, since the set of positive definite 3×3 matrices, Pos(3), cannot be a vector space. Instead, it may be endowed with the structure of a complete Riemannian manifold. Perturbations of order ε^k still make sense in this setting, but one has to interpret the ε^k distance in terms of the metric arising from the Riemannian structure of the manifold Pos(3). In developing perturbations for the conformation tensor, $\mathbf{C}$, we follow the framework of Hameduddin *et al.* (2018, 2019) who focussed on precisely this issue. We may view $\mathbf{C}$ as the left Cauchy-Green tensor associated to the polymer deformation, i.e.,

$$\mathbf{C} = \mathbf{F}\mathbf{F}^T,$$

where $\mathbf{F}$ denotes the deformation gradient with thermal equilibrium taken as the reference configuration. A further decomposition of $\mathbf{F}$ into two successive deformations, which may be written as

$$\mathbf{F} = \mathbf{F}_b\mathbf{L} \tag{2.6}$$

separates the deformation corresponding to the perturbation, $\mathbf{L}$, from the deformation associated with the base state, which may be expressed as†

$$\mathbf{F}_b = \mathbf{C}_b^{\frac{1}{2}}.$$

The fluctuating deformation gradient, $\mathbf{L}$, has an associated left Cauchy-Green tensor $\mathbf{G} = \mathbf{L}\mathbf{L}^T$. Combining these observations, we have that

$$\mathbf{C} = \mathbf{F}_b\mathbf{G}\mathbf{F}_b^T. \tag{2.7}$$

† This representation is not unique, any $\mathbf{F}_b = \mathbf{C}_b^{\frac{1}{2}}\mathbf{R}$ works with $\mathbf{R} \in \mathrm{SO}(3)$. The choice $\mathbf{R} = \mathbf{I}$ is natural in the sense that it allows for a geodesic between $\mathbf{C}_b$ and $\mathbf{C}$ to be expressed solely in terms of $\mathbf{F}_b$ and $\mathbf{G}$.

The tensor $\mathbf{G}$ is necessarily positive definite since $\mathbf{C}$ is, and by nature it acts as the conformation tensor representing the fluctuations of $\mathbf{C}$ around $\mathbf{C}_b$.

The evolution equation (2.1*c*) for the conformation tensor can be rewritten in terms of $\mathbf{G}$ as follows:

$$\partial_t \mathbf{G} + (\mathbf{u}\cdot\boldsymbol{\nabla})\mathbf{G} = 2\mathrm{sym}\left(\mathbf{G}h(\mathbf{u})\right) - \mathbf{F}_b^{-1}\mathbf{T}\mathbf{F}_b^{-T}, \tag{2.8}$$

with

$$h(\mathbf{u}) = \mathbf{F}_b^T\cdot\boldsymbol{\nabla}\mathbf{u}\cdot\mathbf{F}_b^{-T} - \left(\mathbf{F}_b^{-1}(\mathbf{u}\cdot\boldsymbol{\nabla})\mathbf{F}_b\right)^T.$$

As described by Hameduddin *et al.* (2019), an additive expansion of the form (2.5) no longer makes sense on Pos(3), since there is no a priori guarantee that the resulting $\mathbf{C}$ remains positive definite. Instead, Hameduddin *et al.* (2019) proposed a multiplicative expansion based on the decomposition (2.6) that consists of a series of successively smaller deformations, which may be written in the form

$$\mathbf{L}_{wnl} = \mathbf{L}_{(1)}^{\varepsilon}\mathbf{L}_{(2)}^{\varepsilon^2}\cdots\mathbf{L}_{(N)}^{\varepsilon^N}.$$

The matrix $\mathbf{L}_{wnl}$ may differ from $\mathbf{L}$ given in (2.6) by a rotation only.

Under the additional assumption that the $\mathbf{L}_{(k)}^{\varepsilon^k}$ are rotation free with $\det(\mathbf{L}_{(k)}) > 0$, each $\mathbf{L}_k$ is positive definite. The conformation tensors associated to these deformations are then given by $\mathbf{G}_{(k)}^{\varepsilon^k} = \mathbf{L}_{(k)}^{\varepsilon^k}\left(\mathbf{L}_{(k)}^{\varepsilon^k}\right)^T$. To make sense of ε-magnitude perturbations, we make use of the Riemannian manifold structure of Pos(3). In particular, the $\mathbf{G}_{(k)}^{\varepsilon^k}$ may be thought of as length $\sim |\varepsilon|^k$ geodesics emanating from $\mathbf{I}$ on the manifold Pos(3). That is, we may take $\boldsymbol{\mathcal{G}}_{(k)} \in T_{\mathbf{I}}\mathrm{Pos}(3) = \mathrm{Sym}(3)$ such that

$$\mathbf{G}_{(k)}^{\varepsilon^k} = \exp\left(\varepsilon^k\boldsymbol{\mathcal{G}}_{(k)}\right),$$

with

$$d(\mathbf{I}, \mathbf{G}_{(k)}^{\varepsilon^k}) = |\varepsilon|^k\|\boldsymbol{\mathcal{G}}_{(k)}\|_F,$$

where d is the metric induced by the Riemannian structure of Pos(3) ($T_{\mathbf{I}}\mathrm{Pos}(3)$ is the tangent space at the point $\mathbf{I}$ of Pos(3)). Note that this is analogous to weakly nonlinear expansions on vector spaces equipped with the Frobenius norm, only now we measure the corresponding distance on Pos(3) with the Riemannian metric.

This approach eventually leads to an expansion of the form

$$\begin{aligned}\mathbf{G} &= \exp\left(\varepsilon\frac{\boldsymbol{\mathcal{G}}_{(1)}}{2}\right)\cdots\exp\left(\varepsilon^{N-1}\frac{\boldsymbol{\mathcal{G}}_{(N-1)}}{2}\right)\exp\left(\varepsilon^N\boldsymbol{\mathcal{G}}_{(N)}\right)\exp\left(\varepsilon^{N-1}\frac{\boldsymbol{\mathcal{G}}_{(N-1)}}{2}\right)\cdots\exp\left(\varepsilon\frac{\boldsymbol{\mathcal{G}}_{(1)}}{2}\right)\\ &= \mathbf{I} + \varepsilon\boldsymbol{\mathcal{G}}_{(1)} + \varepsilon^2\left(\boldsymbol{\mathcal{G}}_{(2)} + \frac{\boldsymbol{\mathcal{G}}_{(1)}^2}{2}\right) + \varepsilon^3\left(\boldsymbol{\mathcal{G}}_{(3)} + \mathrm{sym}\left(\boldsymbol{\mathcal{G}}_{(1)}\boldsymbol{\mathcal{G}}_{(2)}\right) + \frac{\boldsymbol{\mathcal{G}}_{(3)}^3}{6}\right) + \ldots\end{aligned} \tag{2.9}$$

This representation of the weakly nonlinear terms is equivalent to a standard expansion for $\mathbf{C}$ of the form (2.5), as the operation $\mathbf{G}_{(j)} \mapsto \mathbf{F}_b\mathbf{G}_{(j)}\mathbf{F}_b^T$ serves as a bijection between the two solution sets, as long as $\mathbf{F}_b \in C^0([-1,1];\mathrm{GL}(3))$ i.e. $\mathbf{F}_b$ is a 3×3 invertible matrix with continuous functions in $y \in [-1,1]$ as entries.

While the new formulation does not in practice modify the mechanics of constructing a weakly nonlinear expansion, the mathematical consistency of the approach yields a variety of tools for measuring perturbations on Pos(3) in the only suitable manner, according to the corresponding metric. One such measure, which we shall use frequently in the sections to follow, is the geodesic distance from the mean, given by

$$d(\mathbf{C}_b, \mathbf{C}) = d(\mathbf{I}, \mathbf{G}) = \sqrt{\mathrm{tr}\boldsymbol{\mathcal{G}}^2}. \tag{2.10}$$

3. Weakly nonlinear analysis

Let $\boldsymbol{\varphi} = (u_x, u_y, p, G_{xx}, G_{yy}, G_{zz}, G_{xy})$ denote the vector composed of all state variables. This is further decomposed into two parts: a contribution from the base state and a fluctuating part as follows

$$\boldsymbol{\varphi} = \boldsymbol{\varphi}_b + \hat{\boldsymbol{\varphi}},$$

where the interest is now in solving the governing system (2.1) for the perturbations $\hat{\boldsymbol{\varphi}}$. The Peterlin function (2.1*d*) for $\mathbf{T}$ is first expanded around the base conformation state, $\mathbf{C}_b$ as follows

$$\mathbf{T}(\mathbf{C}) = \mathbf{T}(\mathbf{C}_b) + D\mathbf{T}(\mathbf{C}_b)[\hat{\mathbf{C}}] + \frac{1}{2}D^2\mathbf{T}(\mathbf{C}_b)[\hat{\mathbf{C}}, \hat{\mathbf{C}}] + \frac{1}{6}D^3\mathbf{T}(\mathbf{C}_b)[\hat{\mathbf{C}}, \hat{\mathbf{C}}, \hat{\mathbf{C}}] + \dots. \tag{3.1}$$

For the analysis which follows, it suffices to perform the above expansion (3.1) up to third order and to compress the notation, we shall only consider Wi and Re as varying parameters. The others, β and Sc, are assumed fixed but similar expansions for them may be obtained in an analogous fashion. After a subtraction of the laminar solution, equation (2.1) can be written in an operator form locally around the base state $(\mathbf{u}_b, \mathbf{C}_b)$ as

$$\mathcal{L}\left(Re, Wi\right)[\hat{\boldsymbol{\varphi}}] + \mathcal{B}\left(Re, Wi\right)[\hat{\boldsymbol{\varphi}}, \hat{\boldsymbol{\varphi}}] + \mathcal{T}\left(Re, Wi\right)[\hat{\boldsymbol{\varphi}}, \hat{\boldsymbol{\varphi}}, \hat{\boldsymbol{\varphi}}] = \mathbf{0}, \tag{3.2}$$

where $\mathcal{L}\left(Re, Wi\right)$ is linear, $\mathcal{B}\left(Re, Wi\right)$ is bilinear and $\mathcal{T}\left(Re, Wi\right)$ is symmetric trilinear. These are given explicitly as

$$\mathcal{L}\left(Re, Wi\right)[\hat{\boldsymbol{\varphi}}] = \begin{pmatrix} \partial_t\hat{\mathbf{u}} + (\mathbf{u}_b\cdot\boldsymbol{\nabla})\hat{\mathbf{u}} + (\hat{\mathbf{u}}\cdot\boldsymbol{\nabla})\mathbf{u}_b + \boldsymbol{\nabla}\hat{p} - \frac{\beta}{Re}\Delta\hat{\mathbf{u}} - \frac{1-\beta}{Re}\boldsymbol{\nabla}\cdot\left(D\mathbf{T}(\mathbf{C}_b)\left[\mathbf{F}_b\hat{\mathbf{G}}\mathbf{F}_b^T\right]\right) \\ \boldsymbol{\nabla}\cdot\hat{\mathbf{u}} \\ \partial_t\hat{\mathbf{G}} + (\mathbf{u}_b\cdot\boldsymbol{\nabla})\hat{\mathbf{G}} - 2\mathrm{sym}\left(h\left(\hat{\mathbf{u}}\right) + \hat{\mathbf{G}}h(\mathbf{u}_b)\right) + \mathbf{F}_b^{-1}D\mathbf{T}(\mathbf{C}_b)\left[\mathbf{F}_b\hat{\mathbf{G}}\mathbf{F}_b^T\right]\mathbf{F}_b^{-T} \\ \qquad\qquad - \frac{1}{ReSc}\mathbf{F}_b^{-1}\Delta\left(\mathbf{F}_b\hat{\mathbf{G}}\mathbf{F}_b^T\right)\mathbf{F}_b^{-T} \end{pmatrix},$$

$$\mathcal{B}\left(Re, Wi\right)[\hat{\boldsymbol{\varphi}}_1, \hat{\boldsymbol{\varphi}}_2] = \begin{pmatrix} (\hat{\mathbf{u}}_1\cdot\boldsymbol{\nabla})\hat{\mathbf{u}}_2 - \frac{1-\beta}{2Re}\boldsymbol{\nabla}\cdot\left(D^2\mathbf{T}(\mathbf{C}_b)\left[\mathbf{F}_b\hat{\mathbf{G}}_1\mathbf{F}_b^T, \mathbf{F}_b\hat{\mathbf{G}}_2\mathbf{F}_b^T\right]\right) \\ 0 \\ (\hat{\mathbf{u}}_1\cdot\boldsymbol{\nabla})\hat{\mathbf{G}}_2 - 2\mathrm{sym}\left(\hat{\mathbf{G}}_1h(\hat{\mathbf{u}}_2)\right) + \frac{1}{2}\mathbf{F}_b^{-1}D^2\mathbf{T}(\mathbf{C}_b)\left[\mathbf{F}_b\hat{\mathbf{G}}_1\mathbf{F}_b^T, \mathbf{F}_b\hat{\mathbf{G}}_2\mathbf{F}_b^T\right]\mathbf{F}_b^{-T} \end{pmatrix},$$

$$\mathcal{T}\left(Re, Wi\right)\left[\hat{\boldsymbol{\varphi}}_1, \hat{\boldsymbol{\varphi}}_2, \hat{\boldsymbol{\varphi}}_3\right] = \begin{pmatrix} -\frac{1-\beta}{6Re}\boldsymbol{\nabla}\cdot\left(D^3\mathbf{T}(\mathbf{C}_b)\left[\mathbf{F}_b\hat{\mathbf{G}}_1\mathbf{F}_b^T, \mathbf{F}_b\hat{\mathbf{G}}_2\mathbf{F}_b^T, \mathbf{F}_b\hat{\mathbf{G}}_3\mathbf{F}_b^T\right]\right) \\ 0 \\ \frac{1}{6}\mathbf{F}_b^{-1}D^3\mathbf{T}(\mathbf{C}_b)\left[\mathbf{F}_b\hat{\mathbf{G}}_1\mathbf{F}_b^T, \mathbf{F}_b\hat{\mathbf{G}}_2\mathbf{F}_b^T, \mathbf{F}_b\hat{\mathbf{G}}_3\mathbf{F}_b^T\right]\mathbf{F}_b^{-T} \end{pmatrix}.$$

It's worth remarking that the base state $(\mathbf{u}_b, \mathbf{C}_b)$ in the above operators depends on all parameter values (Wi, Re, β, Sc) through (2.4). Linear stability theory is concerned with the eigenvalue problem arising from the linearized equations, $\mathcal{L}\left(Re, Wi\right)[\hat{\boldsymbol{\varphi}}] = \mathbf{0}$. In practice, this is formally addressed by assuming a specific form of the disturbance, and solving

$$\mathcal{L}\left(Re, Wi\right)\left[\boldsymbol{\varphi}_{(1,1)}(y)\exp(ikx - i\omega t)\right] = 0, \tag{3.3}$$

for pairs $(\omega, \boldsymbol{\varphi}_{(1,1)})$, where $\omega = \omega_r + i\omega_i$ is the *a priori* unknown complex frequency, $\boldsymbol{\varphi}_{(1,1)}$ is the associated eigenmode and k is the prespecified wave number.

Assume now that a bifurcation occurs at a certain triple (Wi_L, Re_L, k), i.e., there exists an eigenmode of (3.3) such that its associated eigenfrequency is real (subsequently denoted by $\omega_L = \omega_{L,r}$), which marks the state of marginal stability in the temporal sense. We wish to uncover how the eigenfunction $\varphi_{(1,1)}$ evolves as we move slightly away from the bifurcation point. For this, consider small perturbations to all relevant parameters of the form

$$(Wi, Re, \omega_r) = (Wi_L, Re_L, \omega_{r,L}) + \varepsilon^2 (Wi_1, Re_1, \omega_{r,1}) + \dots,$$

and formally expand the operator $\mathcal{L}$ around (Re_L, Wi_L) as

$$\mathcal{L}(Re_L + \varepsilon^2 Re_1, Wi_L + \varepsilon^2 Wi_1) = \mathcal{L}(Re_L, Wi_L) + \varepsilon^2 Re_1 \mathcal{L}'_{Re}(Re_L, Wi_L) + \varepsilon^2 Wi_1 \mathcal{L}'_{Wi}(Re_L, Wi_L).$$

The subtle difference here from standard weakly nonlinear expansions lies in the fact that now the base state obtained from (2.4) depends on the parameters Wi and Re. To make this clear and explicit, we write

$$\mathcal{L}'_{Re}(Re_L, Wi_L) = \left.\frac{d}{dRe}\right|_{(Re_L, Wi_L)} \mathcal{L} = \left.\left(\frac{\partial}{\partial Re} + \frac{\partial u_{b,i}}{\partial Re}\frac{\partial}{\partial u_{b,i}} + \frac{\partial F_{b,ij}}{\partial Re}\frac{\partial}{\partial F_{b,ij}}\right)\right|_{(Re_L, Wi_L)} \mathcal{L},$$

$$\mathcal{L}'_{Wi}(Re_L, Wi_L) = \left.\frac{d}{dWi}\right|_{(Re_L, Wi_L)} \mathcal{L} = \left.\left(\frac{\partial}{\partial Wi} + \frac{\partial u_{b,i}}{\partial Wi}\frac{\partial}{\partial u_{b,i}} + \frac{\partial F_{b,ij}}{\partial Wi}\frac{\partial}{\partial F_{b,ij}}\right)\right|_{(Re_L, Wi_L)} \mathcal{L},$$

with

$$\frac{\partial \mathcal{L}}{\partial Re}(Re_L, Wi_L)[\hat{\boldsymbol{\varphi}}] = \begin{pmatrix} \frac{\beta}{Re_L^2}\Delta\hat{\mathbf{u}} + \frac{1-\beta}{Re_L^2}\boldsymbol{\nabla}\cdot\left(D\mathbf{T}(\mathbf{C}_b)\left[\mathbf{F}_b\hat{\mathbf{G}}\mathbf{F}_b^T\right]\right) \\ 0 \\ \frac{1}{Re_L^2 Sc}\mathbf{F}_b^{-1}\Delta\left(\mathbf{F}_b\hat{\mathbf{G}}\mathbf{F}_b^T\right)\mathbf{F}_b^{-T} \end{pmatrix},$$

and

$$\frac{\partial \mathcal{L}}{\partial Wi}(Re_L, Wi_L)[\hat{\boldsymbol{\varphi}}] = \begin{pmatrix} \frac{1-\beta}{Re_L Wi_L}\boldsymbol{\nabla}\cdot\left(D\mathbf{T}(\mathbf{C}_b)\left[\mathbf{F}_b\hat{\mathbf{G}}\mathbf{F}_b^T\right]\right) \\ 0 \\ -\frac{1}{Wi_L}\mathbf{F}_b^{-1}D\mathbf{T}(\mathbf{C}_b)\left[\mathbf{F}_b\hat{\mathbf{G}}\mathbf{F}_b^T\right]\mathbf{F}_b^{-T} \end{pmatrix}.$$

Due to the complexity of the laminar equations (2.4), the base flow's dependence on the parameters is sought numerically, i.e., the terms $\partial u_{b,i}/\partial Re$ and $\partial F_{b,ij}/\partial Re$ - and the corresponding terms in the Wi direction - are computed via a finite difference scheme. We note here that alternatively one could also compute the entirety of $\mathcal{L}'_{Re}$ (and $\mathcal{L}'_{Wi}$) with a finite difference scheme.

To explore how the $\boldsymbol{\varphi}_{(1,1)}$ wave develops as these parameters change, we seek solutions of (3.2) as a weakly nonlinear expansion of the form

$$\boldsymbol{\varphi}(t,x,y) = \boldsymbol{\varphi}_b(y) + \sum_{l=1}^{N}\sum_{q\in J_l}\varepsilon^l\left(\boldsymbol{\varphi}_{(l,q)} + \tilde{\boldsymbol{\varphi}}_{(l,q)}\right)(y)\exp\big(iq(kx-\omega_r t)\big) + O(\varepsilon^{N+1}), \tag{3.4}$$

where $J_l = \{-l, -l+2, \dots, l-2, l\}$, and $\tilde{\boldsymbol{\varphi}}_{(l,q)}$ is the term that represents the dependence of $O(\varepsilon^l)$ perturbations on the lower order $\boldsymbol{\mathcal{G}}_{(j)}$ terms in (2.9). For instance, $\tilde{\boldsymbol{\varphi}}_{(1,q)} = 0$, $q \in \{-1, 1\}$, and

$$\tilde{\boldsymbol{\varphi}}_{(2,2)} = \frac{1}{2}\left(0, 0, 0, \left(\mathcal{G}^2_{(1,1)}\right)_{xx}, \left(\mathcal{G}^2_{(1,1)}\right)_{yy}, \left(\mathcal{G}^2_{(1,1)}\right)_{zz}, \left(\mathcal{G}^2_{(1,1)}\right)_{xy}\right). \tag{3.5}$$

To simplify the notation, let

$$E_q : (t,x) \mapsto \exp\big(iq(kx - \omega_{r,L}t)\big),$$

and

$$\mathcal{L}_q[\boldsymbol{\varphi}] := \mathcal{L}[\boldsymbol{\varphi} E_q].$$

Now, upon substituting the specific form of $\hat{\boldsymbol{\varphi}}$ from Eq. (3.4) into (3.2), we obtain a hierarchy of problems as follows:

$$O(\varepsilon): \quad \mathcal{L}_1[\boldsymbol{\varphi}_{(1,1)}] = \mathbf{0}, \tag{3.6a}$$

$$O(\varepsilon^2): \quad \mathcal{L}_0[\boldsymbol{\varphi}_{(2,0)} + \tilde{\boldsymbol{\varphi}}_{(2,0)}] + \mathcal{B}[\boldsymbol{\varphi}_{(1,1)}E_1, \boldsymbol{\varphi}_{(1,-1)}E_{-1}] + \mathcal{B}[\boldsymbol{\varphi}_{(1,-1)}E_{-1}, \boldsymbol{\varphi}_{(1,1)}E_1] = \mathbf{0}, \tag{3.6b}$$

$$\mathcal{L}_2[\boldsymbol{\varphi}_{(2,2)} + \tilde{\boldsymbol{\varphi}}_{(2,2)}] + \mathcal{B}[\boldsymbol{\varphi}_{(1,1)}E_1, \boldsymbol{\varphi}_{(1,1)}E_1] = \mathbf{0}, \tag{3.6c}$$

$$\begin{aligned} O(\varepsilon^3): \quad & \mathcal{L}_1[\boldsymbol{\varphi}_{(3,1)} + \tilde{\boldsymbol{\varphi}}_{(3,1)}] + \mathcal{B}[\boldsymbol{\varphi}_{(1,-1)}E_{-1}, (\boldsymbol{\varphi}_{(2,2)} + \tilde{\boldsymbol{\varphi}}_{(2,2)})E_2] \\ & + \mathcal{B}[(\boldsymbol{\varphi}_{(2,2)} + \tilde{\boldsymbol{\varphi}}_{(2,2)})E_2, \boldsymbol{\varphi}_{(1,-1)}E_{-1}] + \mathcal{B}[\boldsymbol{\varphi}_{(1,1)}E_1, \boldsymbol{\varphi}_{(2,0)} + \tilde{\boldsymbol{\varphi}}_{(2,0)}] \\ & + \mathcal{B}[\boldsymbol{\varphi}_{(2,0)} + \tilde{\boldsymbol{\varphi}}_{(2,0)}, \boldsymbol{\varphi}_{(1,1)}E_1] + 3\mathcal{T}[\boldsymbol{\varphi}_{(1,1)}E_1, \boldsymbol{\varphi}_{(1,1)}E_1, \boldsymbol{\varphi}_{(1,-1)}E_{-1}] \\ & + Re_1\mathcal{L}'_{Re}[\boldsymbol{\varphi}_{(1,1)}E_1] + Wi_1\mathcal{L}'_{Wi}[\boldsymbol{\varphi}_{(1,1)}E_1] - i\omega_{r,1}\boldsymbol{\varphi}_{(1,1)} =: \mathcal{L}_1[\boldsymbol{\varphi}_{(3,1)}] + \boldsymbol{\eta} = \mathbf{0}, \end{aligned} \tag{3.6d}$$

$$\vdots$$

where $\boldsymbol{\eta}$ is the known part of the last equation (3.6*d*). One subtlety in solving the hierarchy of problems is maintaining the constancy of the volumetric flux. This boils down to introducing a constant correction to the pressure gradient, $\partial_x p_{(2,0)}$, to ensure $\boldsymbol{\varphi}_{(2,0)}$ has zero flux. Provided that the bifurcation is of codimension one, equation (3.6*a*) (equivalent to the linear problem, (3.3)) has a non-unique solution of the form

$$A\frac{\boldsymbol{\varphi}_{(1,1)}}{\|\boldsymbol{\varphi}_{(1,1)}\|_{L^2([-1,1];\mathbb{C}^7)}}, \qquad A \in \mathbb{C}. \tag{3.7}$$

The aim is to map out the possible values of the steady-state amplitude A in the parameter space (Wi, Re). Once an eigenmode of the form (3.7) is pushed through equations (3.6*a*) to (3.6*d*), an explicit solvability condition can be derived, as detailed in the following.

3.1. *Solvability condition*

Let us view the functions $\boldsymbol{\varphi}_{(i,j)} : [-1,1] \to \mathbb{C}^7$ as elements of $L^2\left([-1,1];\mathbb{C}^7\right)$. The inner product on $L^2\left([-1,1];\mathbb{C}^7\right)$ is given by†

$$\langle \boldsymbol{\varphi}, \boldsymbol{\psi} \rangle_{L^2([-1,1];\mathbb{C}^7)} = \int_{[-1,1]} \langle \boldsymbol{\varphi}(y), \boldsymbol{\psi}(y) \rangle_{\mathbb{C}^7}\, dy.$$

The linear problem (3.6*a*) implies that $\mathcal{L}_1$ has a nontrivial kernel. Therefore, the Fredholm alternative theorem implies the existence of a finite dimensional subspace of solutions to the adjoint homogeneous problem

$$\mathcal{L}_1^*[\boldsymbol{\psi}] = \mathbf{0},$$

subject to the appropriate boundary conditions (matching those of the original problem). Moreover, the original equation (3.6*d*) has a solution, $\boldsymbol{\varphi}_{(3,1)}$, if and only if

$$\langle \boldsymbol{\eta}, \boldsymbol{\psi} \rangle_{L^2([-1,1];\mathbb{C}^7)} = 0, \qquad \forall \boldsymbol{\psi} \in \ker \mathcal{L}_1^* \text{ satisfying the boundary conditions.} \tag{3.8}$$

† In the following, we use an L^2 inner product on matrix valued functions as well. In this case, we simply identify the matrices with vectors in the canonical way (i.e., we replace the $\mathbb{C}^7$ inner product below the integral with a Frobenius one).

Assuming that the bifurcation is of codimension one, we know that dim $\left(\ker \mathcal{L}_1^*\right) = 1$, so it suffices to check (3.8) for any $\boldsymbol{\psi}_1 \in \ker \mathcal{L}_1^*$ that satisfies the boundary conditions. With this procedure, we obtain the complex solvability condition

$$aRe_1 + bWi_1 + c|A|^2 + d\omega_{r,1} = 0, \tag{3.9}$$

where

$$\begin{aligned}
a &:= \left\langle \mathcal{L}'_{Re}[\boldsymbol{\varphi}_{(1,1)}E_1], \boldsymbol{\psi}_1 \right\rangle_{L^2\left([-1,1];\mathbb{C}^7\right)} \\
b &:= \left\langle \mathcal{L}'_{Wi}[\boldsymbol{\varphi}_{(1,1)}E_1], \boldsymbol{\psi}_1 \right\rangle_{L^2\left([-1,1];\mathbb{C}^7\right)} \\
c &:= \Big\langle \mathcal{B}[\boldsymbol{\varphi}_{(1,-1)}E_{-1}, (\boldsymbol{\varphi}_{(2,2)} + \tilde{\boldsymbol{\varphi}}_{(2,2)})E_2] + \mathcal{B}[(\boldsymbol{\varphi}_{(2,2)} + \tilde{\boldsymbol{\varphi}}_{(2,2)})E_2, \boldsymbol{\varphi}_{(1,-1)}E_{-1}] \\
&\quad + \mathcal{B}[\boldsymbol{\varphi}_{(1,1)}E_1, \boldsymbol{\varphi}_{(2,0)} + \tilde{\boldsymbol{\varphi}}_{(2,0)}] + \mathcal{B}[\boldsymbol{\varphi}_{(2,0)} + \tilde{\boldsymbol{\varphi}}_{(2,0)}, \boldsymbol{\varphi}_{(1,1)}E_1] \\
&\quad + 3\mathcal{T}[\boldsymbol{\varphi}_{(1,1)}E_1, \boldsymbol{\varphi}_{(1,1)}E_1, \boldsymbol{\varphi}_{(1,-1)}E_{-1}], \boldsymbol{\psi}_1 \Big\rangle_{L^2\left([-1,1];\mathbb{C}^7\right)}, \\
d &:= \left\langle -i\boldsymbol{\varphi}_{(1,1)}, \boldsymbol{\psi}_1 \right\rangle_{L^2\left([-1,1];\mathbb{C}^7\right)}.
\end{aligned}$$

Equation (3.9) gives the desired relationship between the parameters (Wi_1, Re_1) and the steady state amplitude A, which allows us to track how these finite amplitude states emerge from the bifurcation point.

4. Results

As indicated above, we are interested in uncovering the nature of the initial bifurcation associated to the centre-mode instability first identified by Garg *et al.* (2018) in pipe flow and, most relevantly for us, later by Khalid *et al.* (2021*a*) in channel flow. This previous work assumed an Oldroyd-B fluid which allows infinite polymer extension i.e. $L_{max} \to \infty$ for the FENE-P model (2.1*d*). Given this, our objectives in what follows are two-fold. On the one hand, we want to explore the effects of finite extensibility on the aforementioned instability. And on the other, with the aid of the weakly nonlinear analysis, we aim to identify parameter regions where the instability persists beyond the neutral curve to lower Wi in particular.

4.1. $\beta = 0.9$, $L_{max} = 500$ & $Sc \to \infty$

In order to test the weakly nonlinear analysis, we begin by examining the parameter regime considered by Page *et al.* (2020) where $\beta = 0.9$ and $L_{max} = 500$. Using $Sc = 10^3$ to stabilise their time-stepping code, Page *et al.* (2020) observed substantial subcriticality at $(Re, Wi, k) = (60, 26.9, 2)$ on the upper branch of the neutral curve since they were able to continue the branch of solutions down to $Wi = 8.77$. Figure 2 shows the neutral curve at $\beta = 0.9$, $L_{max} = 500$ with $Sc \to \infty$: see appendix A for numerical details. The neutral curve is insensitive to the choice of Sc on the scale of Figure 2 provided it is $\gg 10^2$. Alongside the neutral curve, we display the results of the weakly nonlinear analysis by plotting a curve corresponding to a finite (small) steady state amplitude $|A|$, as obtained from the solvability condition (3.9). The linear instability is a Hopf bifurcation and so the steady state solutions are travelling waves (in x) with phase speed ω_r/k and a constant amplitude which decreases to zero at the neutral curve. This finite amplitude curve in Figure 2 clearly indicates subcriticality along the upper branch of the neutral curve. Proceeding down to the lower branch of the curve, the Hopf bifurcation switches to being supercritical for $Wi \gtrsim 40$ (the red dashed line crosses the black neutral curve).

Figure 2 confirms the subcritical behaviour observed by Page *et al.* (2020) at the point $(Wi, Re, k) \approx (27, 60, 2)$, which is marked by a shaded square □. The corresponding bifurcation diagrams with respect to model parameters Wi and Re are shown in Figure 3. In the

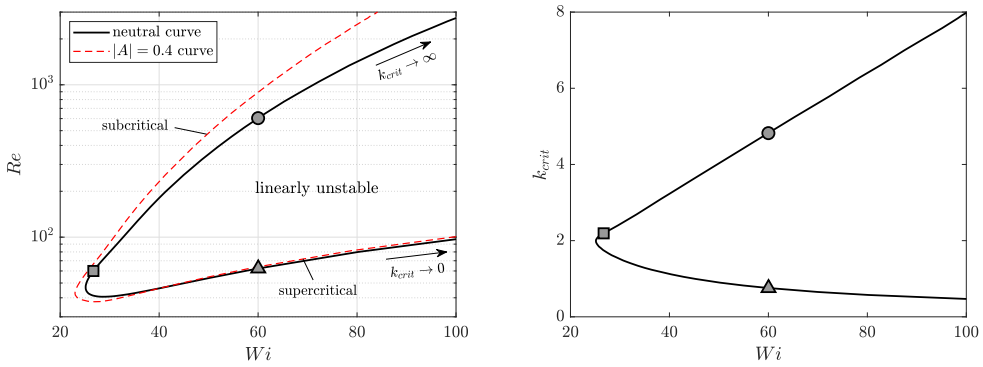

FIGURE 2. (Left) Neutral curve corresponding to marginal linear stability at $\beta = 0.9$, $L_{max} = 500$, $Sc \to \infty$. Results of the weakly nonlinear analysis are shown in the form of a curve at steady state amplitude $|A| = 0.4$. (Right) The development of the critical wave number, k_{crit}, along the neutral curve. Since k_{crit} varies monotonically along the neutral curve its provides a convenient parametrization of it in subsequent figures.

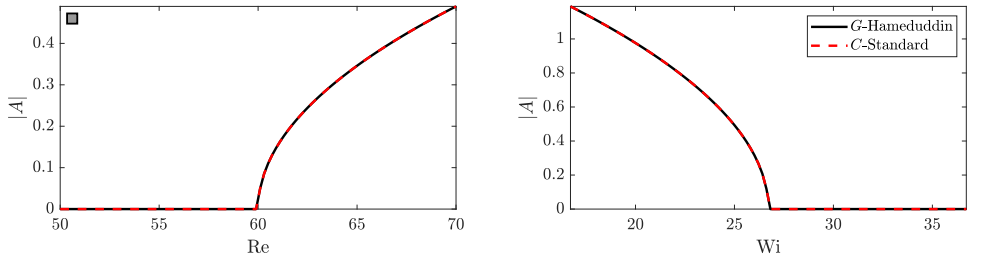

FIGURE 3. Bifurcation diagrams at $(Wi, Re, k) \approx (27, 60, 2)$ (□). Only the unstable branch is displayed with a comparison of two methods for the expansion for the conformation tensor.

figure, the newly developed approach for perturbative expansions of Hameduddin *et al.* (2019) (described in §2.2) is compared with a standard expansion in the conformation tensor, **C**. The two approaches are in clear agreement – a detailed discussion behind the reason for this is given in appendix B. In this context, the real advantage of using the form of expansions established in §2.2 is that we now have immediate access to quantities with tangible physical meaning (cf. Figures 6, 7 and 8).

As a final check, results of the weakly nonlinear analysis are compared with a full branch continuation computation (see appendix A for details of the method) in Figure 4. A finite but large Schmidt number of $Sc = 10^3$ had to be selected for this comparison, as the latter method requires a diffusion term to produce reliable results. The curves are in good agreement - on top of each other near the bifurcation point but then diverging slightly (not visible on the plots) as the amplitude increases (as they should). This divergence, of course, is because the weakly nonlinear analysis is based upon a 3-Fourier-mode expansion whereas the branch continuation curve is from a 40-mode Fourier expansion.

We now examine the bifurcation on the lower branch of the neutral curve for $Wi > 40$ to confirm the supercriticality predicted by the weakly nonlinear analysis. In Figure 5, bifurcation diagrams resulting from the weakly nonlinear analysis for the point △ in Figure 2 are plotted with result from the the Fourier-Chebyshev based branch continuation algorithm. The clear agreement we observe in the vicinity of the critical point confirms the existence of a stable supercritical state, and validates the weakly nonlinear predictions along the lower branch of the neutral curve. A further confirmatory test (backing the initial supercriticality) was performed at a single point

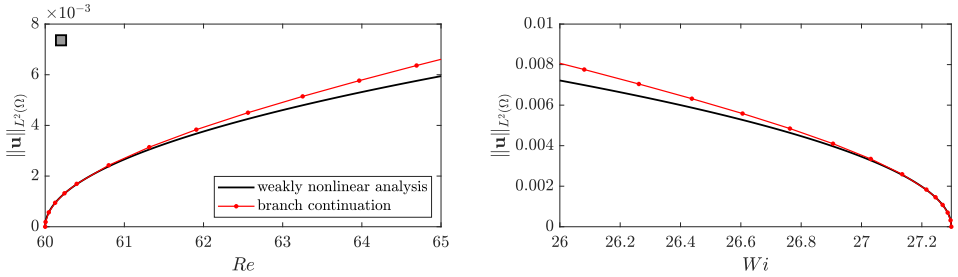

FIGURE 4. Validation of the weakly nonlinear analysis at $(Wi, Re, k) \approx (27, 60, 2)$ (□) with a full branch continuation prediction. The L^2 norms are taken over the whole domain $\Omega = [0, 2\pi/k] \times [-1, 1]$.

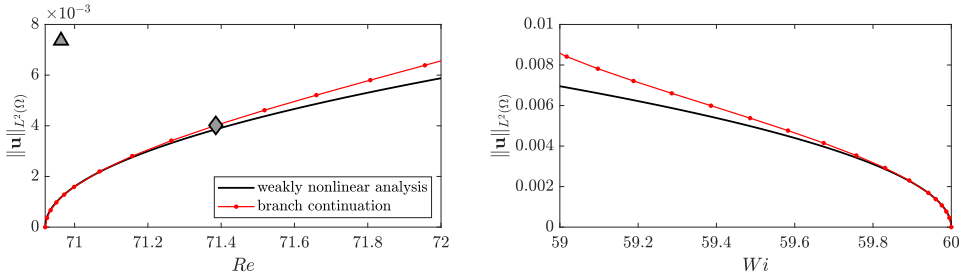

FIGURE 5. Bifurcation diagrams at point △. The L^2 norms are taken over the whole domain $\Omega = [0, 2\pi/k] \times [-1, 1]$.

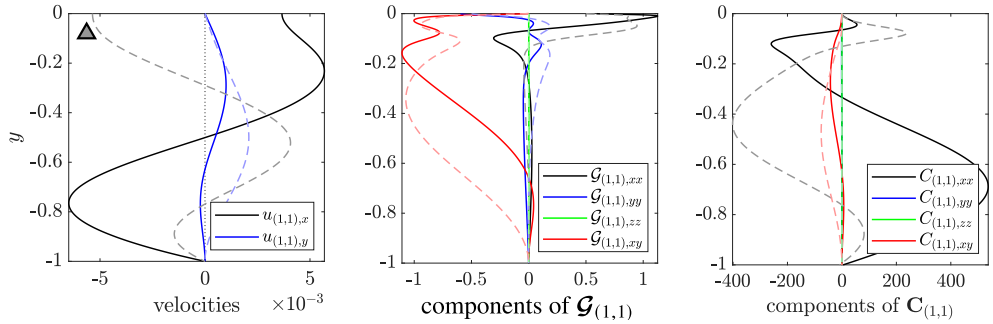

FIGURE 6. Real (——) and imaginary (- - -) parts of the unstable eigenfunction $\boldsymbol{\varphi}_{(1,1)}$ at the point △. (Left) Axial (streamwise) velocity $u_{(1,1),x}$ and vertical velocity $u_{(1,1),y}$. (Middle) All four nonzero components of $\boldsymbol{\mathcal{G}}_{(1,1)} \in T_{\mathbf{I}}\mathrm{Pos}(3)$, the tangent form of the polymer strain perturbation tensor. (Right) All four nonzero components of $\mathbf{C}_{(1,1)} \in \mathrm{Pos}(3)$, the corresponding fluctuation tensor from a standard expansion.

using an independent, finite difference based DNS (the one used in Page *et al.* (2020); Dubief *et al.* (2020); see also §4.3 in Buza *et al.* (2022)).

4.2. *Flow and polymer field prediction*

The various flow and polymer fields generated as part of the weakly nonlinear analysis can be used to generate an approximation to the solution near to a bifurcation point. The structure of the critical eigenfunction at the △ in Figure 2 is shown in Figure 6. The flow and conformation tensor structures are familiar from previous studies (Garg *et al.* 2018; Khalid *et al.* 2021*a*) whereas the Cauchy-Green perturbation tensor $\boldsymbol{\mathcal{G}}_{(1,1)}$ hasn't been shown before. Figure 6 shows that all components of $\boldsymbol{\mathcal{G}}_{(1,1)}$ are confined to the centerline of the channel. For instance, $\mathcal{G}_{(1,1),xx}$ only develops a noticeable magnitude above $y = -0.2$. On the other hand, $C_{(1,1),xx}$ indicates that the

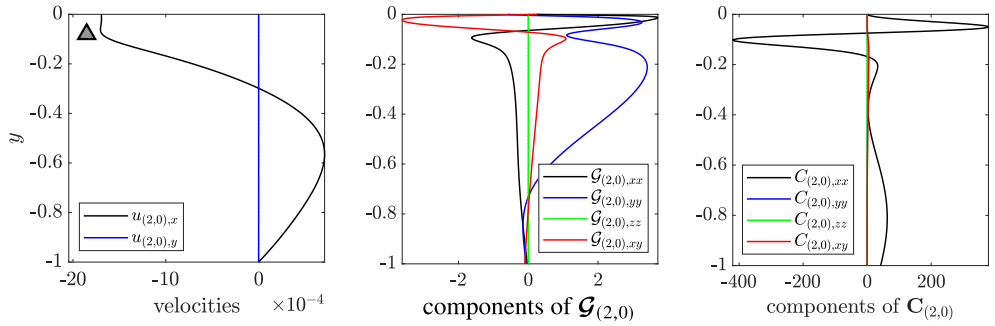

FIGURE 7. The nonlinear mean correction $\boldsymbol{\varphi}_{(2,0)}$ at the point $\triangle$. (Left) Axial (streamwise) velocity $u_{(2,0),x}$ and vertical velocity $u_{(2,0),y} = 0$. (Middle) All four nonzero components of $\boldsymbol{\mathcal{G}}_{(2,0)} \in T_{\mathbf{I}}\mathrm{Pos}(3)$, the mean correction to the conformation tensor in its tangent form. (Right) All four nonzero components of $\mathbf{C}_{(2,0)} \in \mathrm{Pos}(3)$, the corresponding tensor from a standard expansion.

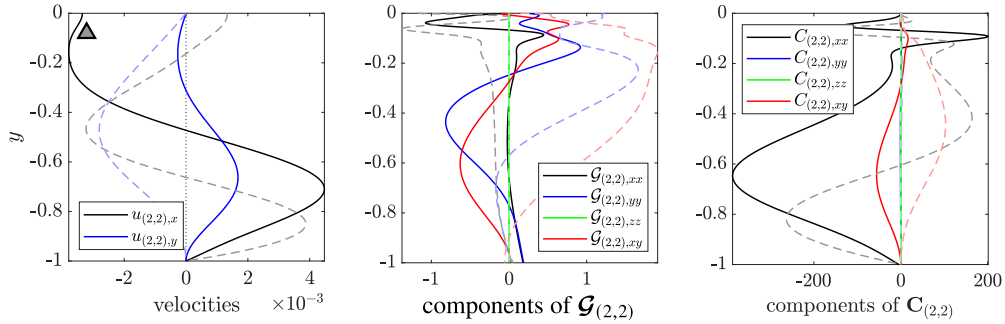

FIGURE 8. Real (——) and imaginary (- - -) parts of the nonlinear correction $\boldsymbol{\varphi}_{(2,2)}$ at the point $\triangle$. (Left) Axial (streamwise) velocity $u_{(2,2),x}$ and vertical velocity $u_{(2,2),y}$. (Middle) All four nonzero components of $\boldsymbol{\mathcal{G}}_{(2,2)} \in T_{\mathbf{I}}\mathrm{Pos}(3)$. (Right) All four nonzero components of $\mathbf{C}_{(2,2)} \in \mathrm{Pos}(3)$, the corresponding tensor from a standard expansion.

streamwise normal stretch reaches its maximum towards the bottom of the channel. This difference is explained by the shape of the laminar base state (cf. Figure 1). $\mathbf{C}_b$ is smaller near the centerline, thus computing $\boldsymbol{\mathcal{G}}_{(1,1)} = \mathbf{F}_b^{-1}\mathbf{C}_{(1,1)}\mathbf{F}_b^{-T}$ amplifies changes in that region, i.e., $\boldsymbol{\mathcal{G}}_{(1,1)}$ recognizes deformations that are large relative to $\mathbf{C}_b$. Again, this is an immediate consequence of the fact that the Riemannian metric on $\mathrm{Pos}(3)$ depends on the base point $\mathbf{C}_b$. Physically, the new formulation highlights that the polymeric disturbance caused by the centre mode instability is confined to a small layer around the centerline, which would not be immediate from a standard expansion in $\mathbf{C}$ (cf. right panel of Figure 6 or Figure 17 in Khalid *et al.* (2021*a*)). Similar observations were reported in the context of transient growth analysis in Zhang (2021) (see Figures 4 and 13 therein).

Higher order disturbances are more difficult to interpret on $\mathrm{Pos}(3)$, but up to $O(\varepsilon^2)$ can still be thought of as consecutive geodesic perturbations (Hameduddin *et al.* 2019). The $O(\varepsilon^2)$ terms from the weakly nonlinear expansion are given in Figure 7, which displays the first nonlinear mean correction $\boldsymbol{\varphi}_{(2,0)}$, and Figure 8, which shows $\boldsymbol{\varphi}_{(2,2)}$. With these fields known, the full flow state can be approximated by evaluating the weakly nonlinear expansion (3.4) up to second order, including $|A|$ in the shape functions as necessary. This low order approximation is compared with a full state from the continuation tool in Figure 9 at the point $\diamond$ on the supercritical bifurcation branch (see Figure 5).

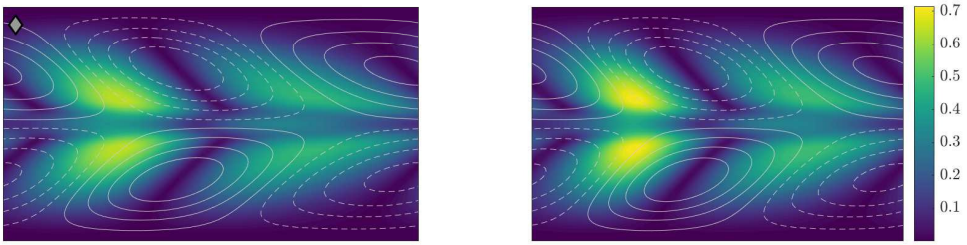

FIGURE 9. Comparison of the supercritical state at point ◇ (identified in Figure 5) as predicted by the weakly nonlinear analysis (left panel) and branch continuation (right panel) techniques. Contours show the geodesic distance between the base and full states $d(C_b, C) = \sqrt{\mathrm{tr}\,\mathcal{G}^2}$, the lines correspond to the perturbation streamfunction.

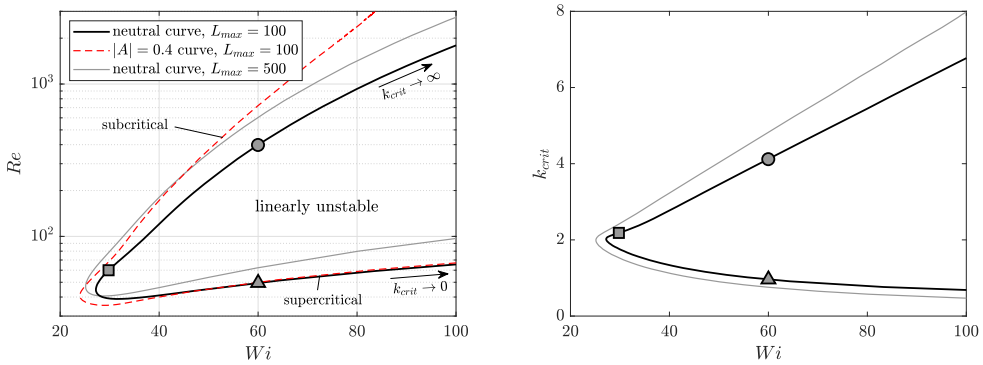

FIGURE 10. (Left) Neutral curve corresponding to marginal linear stability at $\beta = 0.9$, $L_{max} = 100$, $Sc = 10^6$. Results of the weakly nonlinear analysis are shown in the form of a curve at steady state amplitude $|A| = 0.4$. The $L_{max} = 500$ neutral curve from Figure 2 is also shown for comparison. (Right) The development of the critical wave number, k_{crit}, along the neutral curve (corresponding curve for $L_{max} = 500$ again shown in grey).

4.3. $\beta = 0.9$, $L_{max} = 100$ & $Sc = 10^6$

In this subsection, we reduce L_{max} to 100 to explore less extensible (more realistic) polymers and reintroduce the conformation tensor diffusion term into the governing equations (2.1*c*) by considering a finite Schmidt number, $Sc = 10^6$. Figure 10 shows the corresponding marginal stability curve complemented with a finite amplitude curve from the weakly nonlinear analysis. The $L_{max} = 500$ neutral curve is also displayed for comparison in bright grey. All visible changes are caused by the adjustment of L_{max}: the introduction of finite Sc alone has no visual effect. The key observation from Figure 10 is that reducing L_{max} shifts the neutral curve down in Re, and reduces the slope of the lower branch. In particular, lowering L_{max} has a *destabilizing* effect in the elastic regime (low Reynolds numbers). This counter-intuitive finding is the primary motivation for examining the $Re = 0$ instability recently found by Khalid *et al.* (2021*b*) at finite L_{max} in §4.5.

4.4. *Energy analysis*

We now examine the energetic contributions of the different terms in the equations (2.1) in order to examine the mechanisms driving the centre mode instability. This approach has proved useful to diagnose the character of instabilities - for example Joo & Shaqfeh (1991, 1992) identified purely elastic instabilities in curved channel flows with this procedure (see also Zhang *et al.*

(2013) and Agarwal *et al.* (2014)). Taking an L^2 inner product of the momentum equations at $O(\varepsilon)$ and the disturbance velocity field $\mathbf{u}_{(1,1)} = (\boldsymbol{\varphi}_{(1,1),1}, \boldsymbol{\varphi}_{(1,1),2})$ gives (for more details see e.g. Zhang *et al.* 2013) the disturbance kinetic energy equation

$$\partial_t E := \frac{1}{2}\partial_t \|\mathbf{u}_{(1,1)}\|_{L^2}^2 = \mathscr{P} + \mathscr{E} + \mathscr{W}, \tag{4.1}$$

where

$$\mathscr{P} := -\frac{1}{2}\left\langle \boldsymbol{\nabla}\mathbf{u}_b, \mathbf{u}_{(1,1)} \otimes \bar{\mathbf{u}}_{(1,1)} + \bar{\mathbf{u}}_{(1,1)} \otimes \mathbf{u}_{(1,1)} \right\rangle_{L^2}$$

($\bar{\mathbf{u}}$ is the complex conjugate of $\mathbf{u}$) is the disturbance kinetic energy production due to the underlying shear of $\mathbf{u}_b$,

$$\mathscr{E} := -\frac{\beta}{Re}\|\boldsymbol{\nabla}\mathbf{u}_{(1,1)}\|_{L^2}^2$$

represents the viscous dissipation and is strictly negative, and

$$\mathscr{W} := -\frac{(1-\beta)}{2Re}\left(\left\langle \boldsymbol{\nabla}\mathbf{u}_{(1,1)}, \mathbf{T}_{(1,1)} \right\rangle_{L^2} + \left\langle \mathbf{T}_{(1,1)}, \boldsymbol{\nabla}\mathbf{u}_{(1,1)} \right\rangle_{L^2}\right)$$

indicates the rate of work done on the fluid by the polymeric stresses, with

$$\mathbf{T}_{(1,1)} := D\mathbf{T}(\mathbf{C}_b)\left[\mathbf{F}_b \boldsymbol{\mathcal{G}}_{(1,1)} \mathbf{F}_b^T\right].$$

Extending this procedure to identify the mechanisms behind the growth of elastic energy stored in the polymer is well known to be problematic (Doering *et al.* 2006). The underlying issue is that the elastic potential energy, which is a function of $\operatorname{tr}\mathbf{C}$, does not correspond to a norm in the obvious fashion that the kinetic energy does. Once again, this essentially comes down to the fact that the set Pos(3) does not constitute a linear vector space, and there is no notion of norm available. This may be overcome by measuring disturbances in $\mathbf{C}$ along geodesics in Pos(3), according to the metric induced by the Riemannian structure. The work of Hameduddin *et al.* (2018) suggests that

$$(d(\mathbf{C}_b, \mathbf{C}))^2 = (d(\mathbf{I}, \mathbf{G}))^2 = \operatorname{tr}\left(\boldsymbol{\mathcal{G}}^H \boldsymbol{\mathcal{G}}\right),$$

which immediately gives us a way of quantifying the evolution of polymer disturbances as

$$J := \|d(\mathbf{C}_b, \mathbf{C})\|_{L^2}^2 = \int_{[-1,1]} \operatorname{tr}\left(\boldsymbol{\mathcal{G}}^H(y)\boldsymbol{\mathcal{G}}(y)\right)\, dy, \tag{4.2}$$

a formulation which was originally proposed in Hameduddin *et al.* (2019). This, in fact, is the main advantage of relying on the alternative formulation of the governing equations given in equation (2.8). This newly defined quantity J in (4.2) is equal to $\|\boldsymbol{\mathcal{G}}\|_{L^2}^2$ which is a natural generalization of the kinetic energy from (4.1).

Adopting this polymer energy measure J, an energetic evolution equation for the polymer disturbances can now be obtained by taking an L^2 inner product of $\boldsymbol{\mathcal{G}}_{(1,1)}$ with the linearized disturbance equation (in a symmetric fashion) to obtain:

$$\partial_t J = \mathscr{A}_b + \mathscr{A}_1 + \mathscr{T} + \mathscr{E}_p, \tag{4.3}$$

where

$$\mathscr{A}_b := \left\langle \boldsymbol{\mathcal{G}}_{(1,1)}, 2\mathrm{sym}\left(\boldsymbol{\mathcal{G}}_{(1,1)} h(\mathbf{u}_b)\right)\right\rangle_{L^2} + \left\langle 2\mathrm{sym}\left(\boldsymbol{\mathcal{G}}_{(1,1)} h(\mathbf{u}_b)\right), \boldsymbol{\mathcal{G}}_{(1,1)}\right\rangle_{L^2}$$

represents the contribution due to the base velocity field,

$$\mathscr{A}_1 := \left\langle \boldsymbol{\mathcal{G}}_{(1,1)}, 2\mathrm{sym}\left(h\left(\mathbf{u}_{(1,1)}\right)\right)\right\rangle_{L^2} + \left\langle 2\mathrm{sym}\left(h\left(\mathbf{u}_{(1,1)}\right)\right), \boldsymbol{\mathcal{G}}_{(1,1)}\right\rangle_{L^2}$$

is the corresponding term capturing the effect of the disturbance velocity field $\mathbf{u}_{(1,1)}$,

$$\mathscr{T} := -\left\langle \boldsymbol{\mathcal{G}}_{(1,1)}, \mathbf{F}_b^{-1}\mathbf{T}_{(1,1)}\mathbf{F}_b^{-T}\right\rangle_{L^2} - \left\langle \mathbf{F}_b^{-1}\mathbf{T}_{(1,1)}\mathbf{F}_b^{-T}, \boldsymbol{\mathcal{G}}_{(1,1)}\right\rangle_{L^2}$$

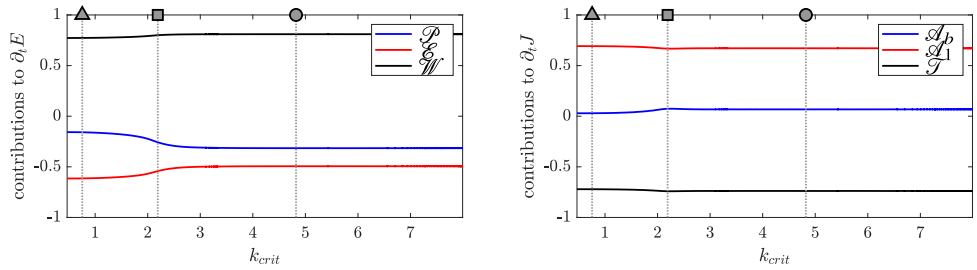

FIGURE 11. Energy analysis results across the $L_{max} = 500$ neutral curve shown in Figure 2. (Left) Components contributing to the production of the turbulent kinetic energy, E. (Right) Components contributing towards the evolution of the polymeric disturbance, J ($\mathscr{E}_p = 0$ for the limit $Sc \to \infty$ considered here and so is not plotted). All values are normalized across the neutral curve.

is the polymeric relaxation term and

$$\mathscr{E}_p := \left\langle \boldsymbol{\mathcal{G}}_{(1,1)}, \frac{1}{ReSc}\mathbf{F}_b^{-1}\Delta\left(\mathbf{F}_b\boldsymbol{\mathcal{G}}_{(1,1)}\mathbf{F}_b^T\right)\mathbf{F}_b^{-T}\right\rangle_{L^2} + \left\langle \frac{1}{ReSc}\mathbf{F}_b^{-1}\Delta\left(\mathbf{F}_b\boldsymbol{\mathcal{G}}_{(1,1)}\mathbf{F}_b^T\right)\mathbf{F}_b^{-T}, \boldsymbol{\mathcal{G}}_{(1,1)}\right\rangle_{L^2}$$

is the polymeric diffusion contribution.

The contribution of each individual term along the neutral curve of subsection 4.1 (parameterised by the wavenumber k_{crit} which varies monotonically along the curve) is shown in Figure 11 for both the kinetic energy equation (4.1) (left) and polymer 'energy' equation (4.3) (right). Based on the recent discovery of an inertialess linear instability that stems from the lower branch of the neutral curve (Khalid *et al.* 2021*b*), it was anticipated that the underlying destabilizing effects would be elastically driven along this branch. This is exactly what is seen: the polymer stress term is the sole energising term for the disturbance kinetic energy. Figure 11, however, indicates that this holds over the upper branch as well so that the centre-mode instability remains purely elastic - i.e., the rate of polymer work $\mathscr{W}$ is the only positive contribution to $\partial_t E$ - throughout the entirety of the neutral curve shown. Not even at $Re = 3000$ do we have a positive contribution from the turbulence production term, $\mathscr{P}$, which is the term that represents inertial effects and is responsible for the onset of instability in Newtonian turbulence. In inertia-dominated flows, $\mathscr{P}$ is the primary cause of turbulent kinetic energy growth Zhang *et al.* (2013).

In the J equation, the base flow ($\mathscr{A}_b$) is positive but barely contributes so that the effect of polymeric relaxation processes, $\mathscr{T}$, is balanced by the input of the perturbation velocity field through $\mathscr{A}_1$ ($\mathscr{E}_p = 0$ as $Sc \to \infty$ and so is not plotted). The dominance of $\mathscr{A}_1$ along the neutral curve is due to the base polymer stretch, rather than via the base flow shear directly.

Choosing large but finite Sc does not change this conclusion. Figure 12 shows the energy analysis results for the neutral curve at $L_{max} = 100$ in Figure 10 of §4.3. Again, the polymeric viscous dissipation term, $\mathscr{E}_p$, does not contribute to the growth of J ($\mathscr{E}_p$ only starts to become significant for $Sc \sim O(10^2)$) and the energy source for the instability is solely elastic.

4.5. *Inertialess limit*

In this section we explore the low-Re elastic limit of the centre mode instability motivated by the finding in §4.3 that decreasing L_{max} makes the instability move to lower Re. Recent work (Khalid *et al.* 2021*b*) has found the centre mode instability for $Re = 0$ in the Oldroyd-B model, albeit at very high Wi and very small $(1-\beta)$ i.e. the dilute limit. Our aim here is to see if we can find this instability at a lower, more realistic Wi by varying L_{max} in the FENE-P model. Taking the limit $Sc \to \infty$ first and then multiplying the momentum equation 2.1*a* through by Re allows

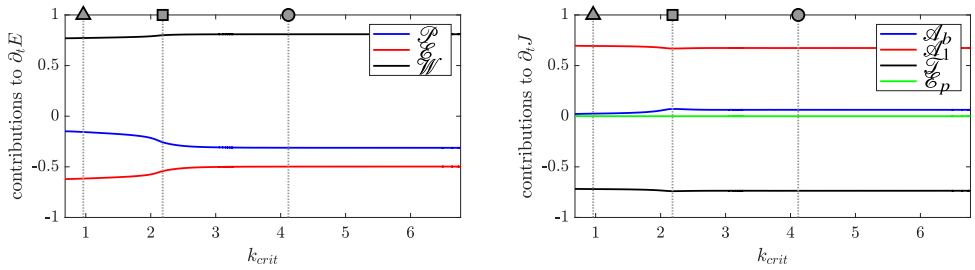

FIGURE 12. Energy analysis results across the $L_{max} = 100$ neutral curve shown in Figure 10. (Left) Components contributing to the production of the turbulent kinetic energy, E. (Right) Components contributing towards the evolution of the polymeric disturbance, J. All values are normalized across the neutral curve.

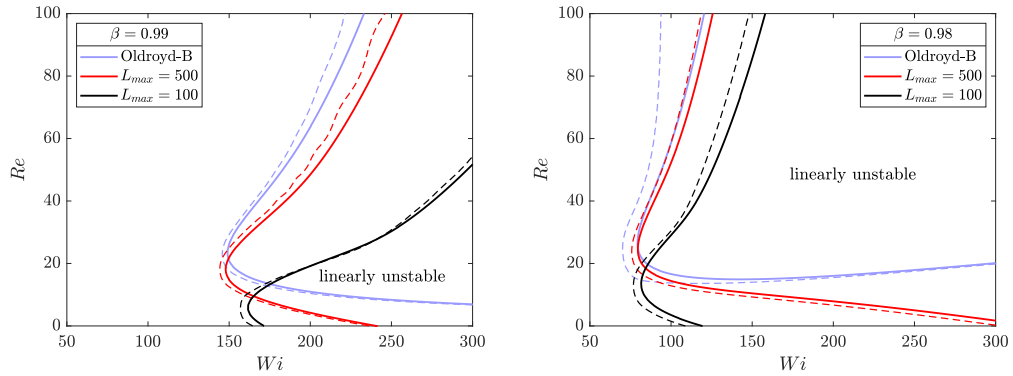

FIGURE 13. Neutrally stable curves (——) around the inertialess ($Re = 0$) limit for ultra-dilute polymer solutions at $\beta = 0.99$ (left) and $\beta = 0.98$ (right). The dashed lines (- - -) are finite amplitude curves that show the nonlinear behaviour indicated by the weakly nonlinear analysis.

the $Re \to 0$ limit to be accessed smoothly. When $Re = 0$, the so-called creeping limit equations,

$$\boldsymbol{\nabla} p = \beta \Delta \mathbf{u} + (1-\beta)\boldsymbol{\nabla} \cdot \mathbf{T}(\mathbf{C}), \tag{4.4a}$$

$$\boldsymbol{\nabla} \cdot \mathbf{u} = 0, \tag{4.4b}$$

$$\partial_t \mathbf{C} + (\mathbf{u} \cdot \boldsymbol{\nabla})\,\mathbf{C} + \mathbf{T}(\mathbf{C}) = \mathbf{C} \cdot \boldsymbol{\nabla}\mathbf{u} + (\boldsymbol{\nabla}\mathbf{u})^T \cdot \mathbf{C}, \tag{4.4c}$$

are reached (see Buza *et al.* (2022) for a different distinguished limit where instead $ReSc$ is kept finite). The effect of the viscosity ratio, β, for $L_{max} \to \infty$ (an Oldroyd-B fluid) is already known (see inset (B) of Figure 2 in Khalid *et al.* 2021*b*). The instability first appears at $\beta = 0.9905$ with the critical Wi decreasing as β increases to 0.994, reaching a minimum of $Wi \approx 649$ (note their value $Wi' = 973.8$ is defined using the base centreline speed) and then increases again as β continues to increase beyond 0.994 towards 1. Thus, the lowest β for which the $Re = 0$ instability still exists (limited by the slope of the lower branch on the marginal curve) could also be decreased if the threshold Wi for instability is decreased through adjusting L_{max}. This is what we find: see figure 13, which shows that instability at $Re = 0$ is possible at just over $Wi = 100$ for $\beta = 0.98$ and $L_{max} = 100$. The finite amplitude curves generated by weakly nonlinear analysis and shown in figure 13 further imply the existence of an unstable subcritical state in this inertialess regime. That is, the flow continues to be nonlinearly unstable when lowering Wi below the threshold for linear instability.

Figure 13 suggests further reduction in the threshold Wi for instability may be possible by making L_{max} even smaller. Neutral curves in the $Wi - \beta$ plane at $Re = 0$ for $L_{max} = 40, 70$ and

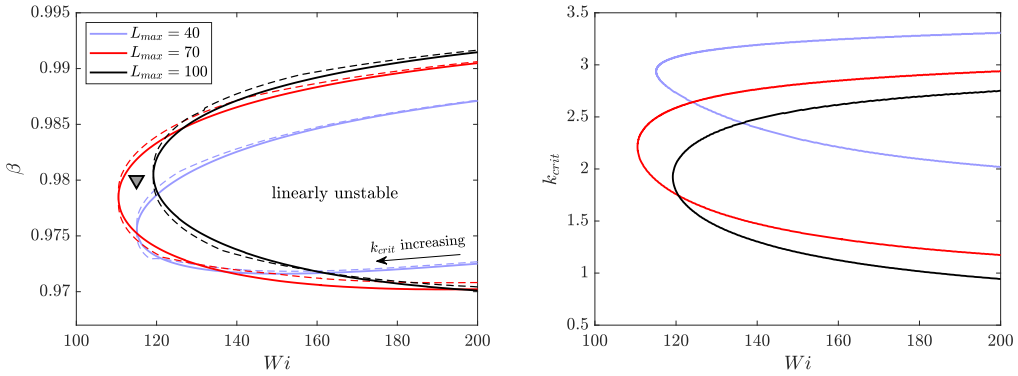

FIGURE 14. (Left) Neutrally stable curves (——) at the inertialess limit $Re = 0$ for ultra-dilute polymer solutions. The dashed lines (- - -) are finite amplitude curves that show the nonlinear behaviour indicated by the weakly nonlinear analysis. (Right) Changes in the critical wave number, k_{crit}, as the neutral curves are traversed.

100 are shown in Figure 14 along with the concomitant finite amplitude curves. Two important features are evident from this figure. Firstly, the destabilizing effect of L_{max} has a limit, which appears to be in the interval $L_{max} \in [40, 100]$ for $Re = 0$. Secondly, the weakly nonlinear analysis indicates that the bifurcation is subcritical with respect to β, except for high Wi along the lower branch (in the $Wi - \beta$ plane) of the neutral curve where it becomes supercritical.

The results of an energy budget analysis are shown in Figure 15 for this $Re = 0$ instability at $Wi = 115$ and $\beta = 0.98$ - the $\triangledown$ in Figure 14 - as a function of L_{max}. The kinetic energy evolution equation (4.1) is unable to handle the vanishing Re situation and so we exclusively focus on the budget in J, the measure introduced for polymeric perturbations. Figure 15 tracks how the disturbance growth rate, $\partial_t J$, and each term contributing to it changes as L_{max} is varied at point $\triangledown$ (cf. Figure 14) ($\partial_t J = 0$ indicate points on the neutral curve e.g. there is no instability at $L_{max} = 100$ at $\triangledown$). The contribution stemming from the base flow, $\mathscr{A}_b$, is still negligible, which indicates that stability is determined by the balance between (destabilizing) $\mathscr{A}_1$ and (stabilizing) $\mathscr{T}$. The dissipation rate associated with polymeric relaxation processes, $\mathscr{T}$, becomes increasing negative as L_{max} is decreased, ultimately causing stabilisation. As expected from Figure 14, an optimal L_{max} exists (≈ 60) for this particular pairing of Wi and β. That it exists at all - i.e. the FENE-P model is *more* unstable than the Oldroyd-B model to this inertialess centre mode instability - is a surprise.

5. Discussion

In this paper, we have considered the character of the bifurcation of a recently-discovered centre-mode (Garg *et al.* 2018; Khalid *et al.* 2021*a*) in rectilinear viscoelastic channel flow for large $Re = O(10^3)$ down to the inertialess limit of $Re = 0$. Using weakly nonlinear analysis within a formal framework which respects the positive definiteness of the conformation tensor $\mathbf{C}$ (Hameduddin *et al.* 2018, 2019), we find that the subcriticality found by Page *et al.* (2020) for one point of the neutral curve at $L_{max} = 500$ is generic across the neutral curve and for different L_{max}. Supercriticality is only found at large Wi on the 'lower' (low-Re) branch of the neutral curve in the (Wi, Re) plane otherwise the branch of travelling waves arising from the neutral curve reach down to lower Wi and the region where EIT is found. In this extended region of parameter space, the base flow is nonlinearly unstable to disturbances of sufficient amplitude. The threshold amplitude to trigger this instability is determined by the minimal amplitude of approach of the stable manifold of the lower branch of travelling waves to the base flow. This is bounded

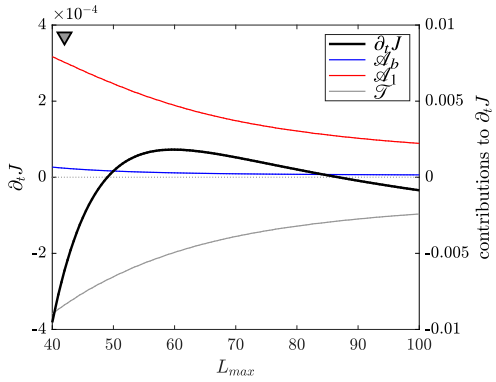

FIGURE 15. The energy budget for the polymeric disturbance, J, at the inertialess limit, at point $\triangledown$ ($Wi = 115$, $\beta = 0.98$) in Figure 14. Note that the scale for $\partial_t J$ (left axis) is enlarged to improve visibility.

from above by the amplitude of the lower branch itself and the one branch-tracking calculation done so far (see Figure 3 in Page *et al.* 2020) indicates that this is small: the volume-averaged tr$\mathbf{C}$ of the travelling wave solutions stays within 5% of the base flow value even when the Wi is reduced to 50% of its value at the bifurcation. Hence, for practical purposes, the base flow may well appear linearly unstable below the neutral curve in Wi (recent experiments suggest a similar situation in Re (Choueiri *et al.* 2021)). Assessing how far this situation continues as Wi is decreased requires, of course, a full branch continuation procedure to map out the surface of travelling wave solutions.

By using a FENE-P fluid we have also confirmed that the centre-mode instability persists for maximum polymer extension down to $L_{max} = 40$ at least. Somewhat counterintuitively, the introduction of finite L_{max} is found to move the neutral curve closer to the inertialess $Re = 0$ limit at fixed β. Pursuing this further by entering the dilute ($\beta \to 1$) limit, we also find that finite L_{max} can bring the linear instability recently found by Khalid *et al.* (2021*b*) down to more physically-relevant $Wi \gtrsim 110$ at $\beta = 0.98$ compared with their threshold of $Wi \approx 649$ (based on the bulk velocity) at $\beta = 0.994$ for $L_{max} \to \infty$. Again the instability is subcritical implying that inertialess rectilinear viscoelastic shear flow is nonlinearly unstable for even lower Wi. Assessing exactly how low again requires locating the saddle node (turning point) of the travelling waves as Wi decreases which requires a branch continuation code.

Finally, by considering the various energy terms in the disturbance kinetic energy equation, we have found that the centre-mode instability is purely elastic in origin even for $Re = O(10^3)$, rather than 'elasto-inertial', as the underlying shear does *not* energise the instability. This finding is consistent with the recent smooth connection found by Khalid *et al.* (2021*b*) to an entirely elastic instability at $Re = 0$ and suggests that EIT and ET may indeed be two different extremes of the same whole. Given that this instability is being suggested as the origin of EIT (Garg *et al.* 2018; Page *et al.* 2020; Chaudhary *et al.* 2021; Khalid *et al.* 2021*a*), the importance of inertia must emerge at finite amplitude and is perhaps already there in the travelling wave solutions especially when they establish their 'arrowhead' form familiar from DNS at higher amplitudes and lower Wi (Dubief *et al.* 2020).

In terms of experiments, the centre mode instability has recently been investigated in both channel (Schnapp & Steinberg 2021) and pipe flow (Choueiri *et al.* 2021). In a pipe, (Choueiri *et al.* 2021) observed evidence of the centre mode instability at high $Wi = O(100)$ and low (subcritical) Re. More relevant to the current results are the essentially inertialess ($Re \lesssim 0.3$) channel flow experiments of Schnapp & Steinberg (2021), which were conducted at very high $Wi \in (100, 1700]$. Finite amplitude traveling waves (or 'elastic' waves in their terminology) were

triggered by 'small' disturbances – in contrast to the 'large' disturbances used in Pan *et al.* (2013) for $Re \lesssim 0.01$ and $Wi \lesssim 10$. Interestingly for the calculations performed here, they estimate the presence of a linear instability at $Wi = 125 \pm 25$. However, both studies were performed at considerably lower values of β than those studied in the bulk of this paper ($\beta = 0.74$ in Schnapp & Steinberg (2021) and $\beta = 0.56$ in Choueiri *et al.* (2021)). We have examined both of these solvent viscosities in Appendix C and find that the significant reduction in β leads to both (i) a smaller unstable region in the Wi-Re plane and (ii) almost uniformly supercritical behaviour around the neutral curve. This does not preclude the possibility that the branch may bend back down towards lower Re and Wi, which cannot be captured in our third order weakly nonlinear analysis but which can be studied by branch continuation of the travelling waves.

The obvious next steps after the analysis described here – and particularly important in the context of the experimental observations at low β – is to employ a branch continuation procedure to track the travelling waves produced by the centre-mode instability to finite amplitudes and then to explore where they exist in parameter space. The inertialess limit is perhaps the most interesting but hardest to access numerically. These travelling waves, of course, provide their own launchpad for further (secondary) bifurcations from which subsequent solutions then suffer tertiary bifurcations and so forth. Establishing that this bifurcation cascade occurs precisely where EIT is observed in parameter space would provide convincing evidence of the importance of the centre-mode instability. We hope to report on further progress in this direction in the near future (see Buza *et al.* (2022)).

Acknowledgements: GB gratefully acknowledges the support of the Harding Foundation through a PhD scholarship (https://www.hardingscholars.fund.cam.ac.uk).

Declaration of Interests. The authors report no conflict of interest.

Appendix A. Numerical methods

The eigenvalue problem (3.6*a*) and the subsequent nonlinear equations in (3.6) were solved using a Chebyshev discretization (for the special case of $Re = 0$, the operators in (3.6) were based on the creeping equations instead as discussed in the main text). Exploiting the symmetries of the centre eigenmode, the expansions were performed over half the channel width, $y \in [-1, 0]$, with appropriate boundary conditions to enforce the symmetry of u_x, antisymmetry of u_y and appropriate symmetries for the various components of $\mathbf{C}$. This approach crucially concentrates the collocation points near *both* the channel boundary and the centreline where the eigenmode is localised so that manageable truncations prove adequate. For the $\beta = 0.9$ neutral curves, 200 Chebyshev were sufficient while higher β values needed 300-400 Chebyshev modes due to the increasing localization of the unstable eigenmode (see Khalid *et al.* (2021*b*)). The neutral curves were obtained using a continuation scheme that relies on the tangent that the weakly nonlinear analysis yields. Specifically, in the $Wi - Re$ plane, this is given by substituting $|A| = 0$ into (3.9):

$$\frac{Re_1}{Wi_1} = -\frac{\mathrm{Im}(\bar{d}b)}{\mathrm{Im}(\bar{d}a)}.$$

In solving the eigenvalue problem, a shift-inverse spectral transformation Meerbergen *et al.* (1994) was employed, using the eigenvalue at the previous continuation step, to isolate the critical eigenmode. The unstable mode was then obtained via standard power iteration. All results were cross-checked using two grid resolutions.

Results of the weakly nonlinear analysis were validated by an independently-developed branch continuation routine. In this, the flow solution is assumed to be steady in an appropriately-chosen Galilean frame (i.e. a travelling wave) which allows the time derivatives to be replaced by a spatial derivative in x premultiplied by an *a priori* unknown phase speed $c = \omega_r/k$. The governing equations are then discretized in space using Fourier modes in x and Chebyshev modes in y across the domain $(x, y) \in [0, 2\pi/k] \times [-1, 1]$ to leave a high-dimensional - typically $O(10^5)$ degrees of freedom - nonlinear system of equations for the expansion coefficients. A good starting guess for the solution and c can be generated near the neutral curve and then the solver propagates along the solution surface via a pseudo-arclength continuation algorithm based on a Newton-Raphson iterative scheme (e.g. Dijkstra *et al.* (2014)). Simulations for the curves appearing in Figures 4 and 5 were run at 80 Chebyshev and 40 Fourier modes (so $7 \times 40 \times 80 \times 2 = 44,800$ real degrees of freedom). Resolution independence was carefully checked at the terminal point of each branch shown (using up to 80,000 degrees of freedom). In this paper, the branch continuation code was only used to confirm the weakly nonlinear analysis. A future report will describe it in detail when the results of using it to explore solution morphology a finite distance from the neutral curve will be presented.

Appendix B. Equivalence of the G and C formulations for weakly nonlinear analysis

In this appendix, we show the equivalence of the **G** and **C** formulations in the context of weakly nonlinear analyses. The only assumption required for this is

$$\mathbf{F}_b \in C^0\big([-1, 1]; \mathrm{GL}(3)\big), \tag{B 1}$$

which is fulfilled for any positive definite solution $\mathbf{C}_b$ of (2.4) due to physical considerations ($\det(\mathbf{F}_b(y)) = 0$ would imply that material elements are compressed to zero volume). Let us denote by $\mathcal{K} : L^2\left([-1, 1]; \mathbb{C}^7\right) \to L^2\left([-1, 1]; \mathbb{C}^7\right)$ the map translating between the two formulations, i.e.†

$$\mathcal{K} : (\mathbf{u}, p, \mathrm{vec}(\mathbf{G})) \mapsto (\mathbf{u}, p, \mathrm{vec}(\mathbf{F}_b \mathbf{G} \mathbf{F}_b^T)).$$

Then $\mathcal{K}$ is a bounded linear operator by (B 1), with a bounded inverse $\mathcal{K}^{-1}$.

Governing equations for **C** (2.1) may now be obtained upon applying $\mathcal{K}$ to the equations for **G** (cf. (2.8)). Revisiting the sequence of problems arising in weakly nonlinear theory (3.6), now in

† The operation vec sends **G** to $(\mathbf{G}_{xx}, \mathbf{G}_{yy}, \mathbf{G}_{zz}, \mathbf{G}_{xy})$.

the **C** formulation with $\boldsymbol{\varphi}^{\mathbf{C}} := (u_x, u_y, p, C_{xx}, C_{yy}, C_{zz}, C_{xy})$ yields

$$O(\varepsilon): \quad \mathcal{K}\mathcal{L}_1\mathcal{K}^{-1}[\boldsymbol{\varphi}^{\mathbf{C}}_{(1,1)}] = \mathbf{0}, \tag{B 2a}$$

$$O(\varepsilon^2): \quad \mathcal{K}\mathcal{L}_0\mathcal{K}^{-1}[\boldsymbol{\varphi}^{\mathbf{C}}_{(2,0)}] + \mathcal{K}\mathcal{B}[\mathcal{K}^{-1}\boldsymbol{\varphi}^{\mathbf{C}}_{(1,1)}E_1, \mathcal{K}^{-1}\boldsymbol{\varphi}^{\mathbf{C}}_{(1,-1)}E_{-1}] + \mathcal{K}\mathcal{B}[\mathcal{K}^{-1}\boldsymbol{\varphi}^{\mathbf{C}}_{(1,-1)}E_{-1}, \mathcal{K}^{-1}\boldsymbol{\varphi}^{\mathbf{C}}_{(1,1)}E_1] = \mathbf{0}, \tag{B 2b}$$

$$\mathcal{K}\mathcal{L}_2[\mathcal{K}^{-1}\boldsymbol{\varphi}^{\mathbf{C}}_{(2,2)}] + \mathcal{K}\mathcal{B}[\mathcal{K}^{-1}\boldsymbol{\varphi}^{\mathbf{C}}_{(1,1)}E_1, \mathcal{K}^{-1}\boldsymbol{\varphi}^{\mathbf{C}}_{(1,1)}E_1] = \mathbf{0}, \tag{B 2c}$$

$$\begin{aligned} O(\varepsilon^3): \quad & \mathcal{K}\mathcal{L}_1[\mathcal{K}^{-1}\boldsymbol{\varphi}^{\mathbf{C}}_{(3,1)}] + \mathcal{K}\mathcal{B}[\mathcal{K}^{-1}\boldsymbol{\varphi}^{\mathbf{C}}_{(1,-1)}E_{-1}, \mathcal{K}^{-1}\boldsymbol{\varphi}^{\mathbf{C}}_{(2,2)}E_2] \\ & + \mathcal{K}\mathcal{B}[\mathcal{K}^{-1}\boldsymbol{\varphi}^{\mathbf{C}}_{(2,2)}E_2, \mathcal{K}^{-1}\boldsymbol{\varphi}^{\mathbf{C}}_{(1,-1)}E_{-1}] + \mathcal{K}\mathcal{B}[\mathcal{K}^{-1}\boldsymbol{\varphi}^{\mathbf{C}}_{(1,1)}E_1, \mathcal{K}^{-1}\boldsymbol{\varphi}^{\mathbf{C}}_{(2,0)}] \\ & + \mathcal{K}\mathcal{B}[\mathcal{K}^{-1}\boldsymbol{\varphi}^{\mathbf{C}}_{(2,0)}, \mathcal{K}^{-1}\boldsymbol{\varphi}^{\mathbf{C}}_{(1,1)}E_1] \\ & + 3\mathcal{K}\mathcal{T}[\mathcal{K}^{-1}\boldsymbol{\varphi}^{\mathbf{C}}_{(1,1)}E_1, \mathcal{K}^{-1}\boldsymbol{\varphi}^{\mathbf{C}}_{(1,1)}E_1, \mathcal{K}^{-1}\boldsymbol{\varphi}^{\mathbf{C}}_{(1,-1)}E_{-1}] \\ & + Re_1\mathcal{K}\mathcal{L}'_{Re}[\mathcal{K}^{-1}\boldsymbol{\varphi}^{\mathbf{C}}_{(1,1)}E_1] + Wi_1\mathcal{K}\mathcal{L}'_{Wi}[\mathcal{K}^{-1}\boldsymbol{\varphi}^{\mathbf{C}}_{(1,1)}E_1] - i\omega_{r,1}\boldsymbol{\varphi}^{\mathbf{C}}_{(1,1)} = \mathbf{0}, \end{aligned} \tag{B 2d}$$

$$\vdots$$

At first order, we have

$$\ker\left(\mathcal{K}\mathcal{L}_1\mathcal{K}^{-1}\right) = \mathcal{K}\ker\mathcal{L}_1,$$

which is of complex dimension one on the neutral curve, so that $\boldsymbol{\varphi}^{\mathbf{C}}_{(1,1)} = \mathcal{K}\boldsymbol{\varphi}_{(1,1)}$ up to complex multiplication (this degree of freedom is eliminated upon imposing (3.7)), establishing equivalence at the level of linear stability. Substituting this into equations at second order and comparing them with their **G** counterparts (3.6), we obtain

$$\boldsymbol{\varphi}^{\mathbf{C}}_{(2,0)} = \mathcal{K}\left(\boldsymbol{\varphi}_{(2,0)} + \tilde{\boldsymbol{\varphi}}_{(2,0)}\right), \quad \text{and} \quad \boldsymbol{\varphi}^{\mathbf{C}}_{(2,2)} = \mathcal{K}\left(\boldsymbol{\varphi}_{(2,2)} + \tilde{\boldsymbol{\varphi}}_{(2,2)}\right). \tag{B 3}$$

Since $\mathcal{K}$ is an isomorphism and the $\tilde{\boldsymbol{\varphi}}$ parts are already known (cf. (3.5)), (B 3) establishes equivalence at second order. At third order, a solvability condition is derived (see §3.1) upon taking the inner product of (B 2*d*) with a nonzero element of the kernel of the adjoint problem. In the **C** formulation, the adjoint kernel takes the form

$$\ker\left(\mathcal{K}\mathcal{L}_1\mathcal{K}^{-1}\right)^* = \ker\left((\mathcal{K}^{-1})^*\mathcal{L}_1^*\mathcal{K}^*\right) = (\mathcal{K}^{-1})^*\ker\mathcal{L}_1^*,$$

thus, $\boldsymbol{\psi}^{\mathbf{C}}_1 = (\mathcal{K}^{-1})^*\boldsymbol{\psi}_1$ up to complex multiplication (which is irrelevant because the entire equation will be multiplied with it). Taking the inner product with $\boldsymbol{\psi}^{\mathbf{C}}_1$, any term of (B 2*d*) will behave similarly to

$$\begin{aligned} &\left\langle Re_1\mathcal{K}\mathcal{L}'_{Re}[\mathcal{K}^{-1}\boldsymbol{\varphi}^{\mathbf{C}}_{(1,1)}E_1], (\mathcal{K}^{-1})^*\boldsymbol{\psi}_1\right\rangle_{L^2([-1,1];\mathbb{C}^7)} \\ &\qquad = Re_1\left\langle\mathcal{L}'_{Re}[\boldsymbol{\varphi}_{(1,1)}E_1], \boldsymbol{\psi}_1\right\rangle_{L^2([-1,1];\mathbb{C}^7)} = Re_1 a. \end{aligned} \tag{B 4}$$

In the nonlinear terms, the same conclusion is reached once (B 3) is substituted. Thus, a, b, c and d are unchanged in the solvability condition (3.9).

Perhaps a more 'natural' inner product for the **G** formulation is obtained upon replacing the $\mathbb{C}^7$ inner product under the L^2 integral with a Frobenius one (equivalent to taking the $\boldsymbol{\mathcal{G}}_{xy}$ component twice), given that the Riemannian metric reduces to the Frobenius inner product at the base of perturbations, $\mathbf{I} \in \mathrm{Pos}(3)$. This change is compensated for by the adjoint kernel similarly to (B 4), leaving the resulting solvability condition (3.9) unchanged.

Note that the above procedure in (B 3) can be continued up to arbitrary order, thereby making generalized weakly nonlinear theories independent of the chosen formulation as well.

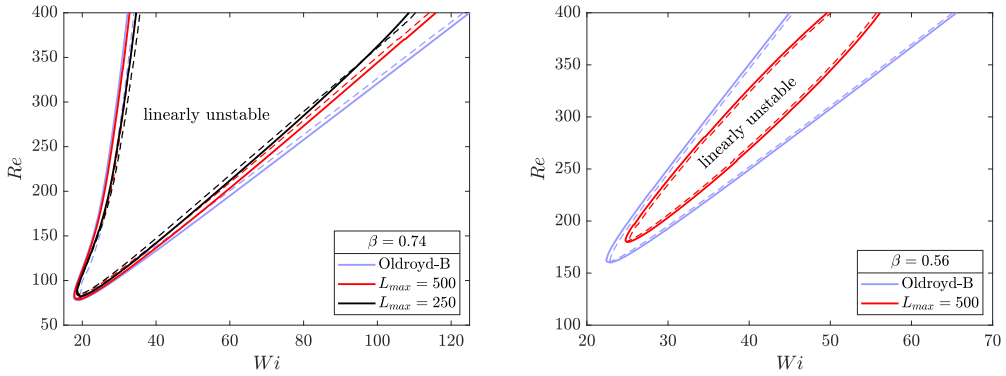

FIGURE 16. Neutrally stable curves (——) for low solvent viscosities $\beta = 0.74$ (left) and $\beta = 0.56$ (right). The dashed lines (- - -) are finite amplitude curves that show the nonlinear behaviour indicated by the weakly nonlinear analysis.

The **G** formulation does make a difference, however, in scenarios where the novel perturbation measures are directly incorporated into the analysis. For instance, the use of (4.2) in the energy analysis §4.4 changes proportions in the polymeric energy balance. Another such example is transient growth analysis, recently explored using the **G** formulation in pipe flows (Zhang 2021), which clearly depends on the choice of norm used in the objective functional.

Appendix C. Results at moderate β

Motivated by recent experimental results (Choueiri *et al.* 2021; Schnapp & Steinberg 2021) at higher polymer concentrations, we briefly discuss the impact of reducing β on both the linear instability and the predictions of our weakly nonlinear analysis. We consider two solvent viscosities, $\beta = 0.74$ and $\beta = 0.56$, which match the values obtained in Schnapp & Steinberg (2021) and Choueiri *et al.* (2021) respectively (note the latter study was done in a pipe precluding any direct comparison here). Neutral curves and the weakly nonlinear results are reported in figure 16 for both Oldroyd-B fluids and FENE-P fluid with relatively high L_{max}. The reduction in β noticably shrinks the region of instability in the Wi-Re plane, notably bending the lower part of the curve - which connects to $Re = 0$ at high β - upwards. Moreover, in contrast to the dilute ($\beta \geqslant 0.9$) results in the bulk of this paper, the introduction of finite extensibility has a uniformly stabilizing effect – this behaviour is perhaps more typical of the more realistic polymer model; in many cases the reduction in the base-state normal stress tends to suppress more 'interesting' Oldroyd-B results (e.g. see the linear analyses in Ray & Zaki 2014; Page & Zaki 2015).

In addition, the weakly nonlinear results (dashed lines in figure 16) indicate almost uniformly supercritical behaviour around the neutral curve (note the small exception at high Wi for $\beta = 0.74$ and $L_{max} = 250$). This finding should be contrasted to the recent experimental results at extreme $Wi \geqslant 100$ of Schnapp & Steinberg (2021), who have observed finite amplitude traveling waves at very low Re at $\beta = 0.74$, and motivates further study via branch continuation of exactly where nonlinear traveling waves are predicted to exist in the parameter space.

REFERENCES

AGARWAL, A., BRANDT, L. & ZAKI, T. A. 2014 Linear and nonlinear evolution of a localized disturbance in polymeric channel flow. *Journal of Fluid Mechanics* **760**, 278–303.

BUZA, G., BENEITEZ, M., PAGE, J. & KERSWELL, R. R. 2022 Finite-amplitude elastic waves in viscoelastic channel flow from large to zero Reynolds number. *arXiv:2202.08047* .

Chandra, B., Shankar, V. & Das, D. 2018 Onset of transition in the flow of polymer solutions in microtubes. *Journal of Fluid Mechanics* **844**, 1052–1083.

Chaudhary, Indersh, Garg, Piyush, Shankar, V. & Subramanian, Ganesh 2019 Elasto-inertial wall mode instabilities in viscoelastic plane Poiseuille flow. *Journal of Fluid Mechanics* **881**, 119–163.

Chaudhary, I., Garg, P., Subramanian, G. & Shankar, V. 2021 Linear instability of viscoelastic pipe flow. *Journal of Fluid Mechanics* **908**, A11.

Choueiri, G. H., Lopez, J. M. & Hof, B. 2018 Exceeding the Asymptotic Limit of Polymer Drag Reduction§. *Physical Review Letters* **120**, 124501.

Choueiri, G. H., Lopez, J. M., Varshey, A., Sankar, S. & Hof, B. 2021 Experimental observation of the origin and structure of elasto-inertial turbulence. *Proceedings of the National Academy of Sciences of the United States* **118**, e2102350118.

Dijkstra, Henk A., Wubs, Fred W., Cliffe, Andrew K., Doedel, Eusebius, Dragomirescu, Ioana F., Eckhardt, Bruno, Gelfgat, Alexander Yu., Hazel, Andrew L., Lucarini, Valerio, Salinger, Andy G. & et al. 2014 Numerical bifurcation methods and their application to fluid dynamics: Analysis beyond simulation. *Communications in Computational Physics* **15** (1), 1–45.

Doering, C. R., Eckhardt, B. & Schumacher, J. 2006 Failure of energy stability in Oldroyd-B fluids at arbitrarily low Reynolds numbers. *Journal of Non-Newtonian Fluid Mechanics* **135**, 92–96.

Draad, A. A., Kuiken, G. D. C. & Nieuwstadt, F. T. M. 1998 Laminar-turbulent transition in pipe flow for Newtonian and non-Newtonian fluids. *Journal of Fluid Mechanics* **377**, 267–312.

Dubief, Y., Page, J., Kerswell, R. R., Terrapon, V. E. & Steinberg, V. 2020 A first coherent structure in elasto-inertial turbulence. *arXiv 2006.06770* .

Dubief, Y., Terrapon, V. E. & Soria, J. 2013 On the mechanism of elasto-inertial turbulence. *Physics of Fluids* **25** (11), 110817.

Garg, P., Chaudhary, I., Khalid, M., Shankar, V. & Subramanian, G. 2018 Viscoelastic Pipe Flow is Linearly Unstable. *Physical Review Letters* **121**, 024502.

Goldstein, R. J., Adrian, R. J. & Kreid, D. K. 1969 Turbulent and transition pipe flow of dilute aqueous polymer solutions. *Industrial and Engineering Chemistry Fundamentals* **8**, 498.

Graham, M. D. 2014 Drag reduction and the dynamics of turbulence in simple and complex fluids. *Physics of Fluids* **26**, 101301.

Groisman, A. & Steinberg, V. 2000 Elastic turbulence in a polymer solution flow. *Nature* **405**, 53–55.

Hameduddin, Ismail, Gayme, Dennice F. & Zaki, Tamer A. 2019 Perturbative expansions of the conformation tensor in viscoelastic flows. *Journal of Fluid Mechanics* **858**, 377–406.

Hameduddin, Ismail, Meneveau, Charles, Zaki, Tamer A. & Gayme, Dennice F. 2018 Geometric decomposition of the conformation tensor in viscoelastic turbulence. *Journal of Fluid Mechanics* **842**, 395–427.

Hansen, R. J. & Little, R. C. 1974 Early turbulence and drag reduction phenomena in larger pipes. *Nature* **252**, 690.

Jones, W. & Maddock, J. L. 1966 Onset of instabilities and reduction of drag in flow of relaxing liquids through tubes and porous beds. *Nature* **212**, 388.

Joo, Yong Lak & Shaqfeh, Eric S. G. 1991 Viscoelastic poiseuille flow through a curved channel: A new elastic instability. *Physics of Fluids A: Fluid Dynamics* **3** (7), 1691–1694.

Joo, Y. L. & Shaqfeh, E. S. G. 1992 A purely elastic instability in Dean and Taylor-Dean flow. *Physics of Fluids* **4**, 524.

Jovanović, M. R. & Kumar, S. 2010 Transient growth without inertia. *Physics of Fluids* **22**, 023101.

Jovanović, M. R. & Kumar, S. 2011 Nonmodal amplification of stochastic disturbances in strongly elastic channel flows. *Journal of Non-Newtonian Fluid Mechanics* **166**, 755–778.

Khalid, Mohammad, Chaudhary, Indresh, Garg, Piyush, Shankar, V. & Subramanian, Ganesh 2021*a* The centre-mode instability of viscoelastic plane poiseuille flow. *Journal of Fluid Mechanics* **915**, A43.

Khalid, Mohammad, Shankar, V. & Subramanian, Ganesh 2021*b* A continuous pathway between the elasto-inertial and elastic turbulent states in viscoelastic channel flow. *Phys. Rev. Lett.* **127**, 134502.

Larson, R. G., Shaqfeh, E. S. G. & Muller, S. J. 1990 A purely elastic instability in Taylor-Couette flow. *Journal of Fluid Mechanics* **218**, 573–600.

Lopez, J. M., Choueiri, George H. & Hof, Bjoern 2019 Dynamics of viscoelastic pipe flow at low Reynolds numbers in the maximum drag reduction limit. *Journal of Fluid Mechanics* **874**, 699–719.

Lumley, J. L. 1969 Drag reduction by additives. *Annual Review of Fluid Mechanics* **656** (33), 367–384.

Meerbergen, Karl, Spence, A & Roose, Dirk 1994 Shift-invert and cayley transforms for detection of rightmost eigenvalues of nonsymmetric matrices. *Bit Numerical Mathematics* **34** (3), 409–423.

Meulenbroek, B., Storm, C., Morozov, A. N. & van Saarloos, W. 2004 Weakly nonlinear subcritical instability of visco-elastic Poiseuille flow. *Journal of Non-Newtonian Fluid Mechanics* **116** (2-3), 235–268.

Morozov, A. N. & Saarloos, W. V. 2007 An introductory essay on subcritical instabilities and the transition to turbulence in visco-elastic parallel shear flows. *Physics Reports* **447**, 112–143.

Page, Jacob, Dubief, Yves & Kerswell, Rich R. 2020 Exact traveling wave solutions in viscoelastic channel flow. *Phys. Rev. Lett.* **125**, 154501.

Page, J. & Zaki, T. A. 2015 The dynamics of spanwise vorticity perturbations in homogeneous viscoelastic shear flow. *Journal of Fluid Mechanics* **777**, 327–363.

Pan, L., Morozov, A., Wagner, C. & Arratia, P. E. 2013 Nonlinear elastic instability in channel flows at low Reynolds numbers. *Physical Review Letters* **110**, 174502.

Procaccia, I., Lvov, Victor & Benzi, Roberto 2008 Colloquium: Theory of drag reduction by polymers in wall-bounded turbulence. *Reviews of Modern Physics* **1**, 225–247.

Qin, B. Y., Salipante, P. F., Hudson, S. D. & Arratia, P. E. 2019 Flow resistance and structure in viscoelastic channel flows at low Re. *Physical Review Letters* **123**, 194501.

Ray, P. K. & Zaki, T. A. 2014 Absolute instability in viscoelastic mixing layers. *Physics of Fluids* **26** (1), 014103.

Samanta, D. S., Dubief, Y., Holzner, H., Schäfer, C., Morozov, A. N., Wagner, C. & Hof, B. 2013 Elasto-inertial turbulence. *Proceedings of the National Academy of Sciences of the United States of America* **110**, 10557–10562.

Sanchez, H. A. Castillo, Jovanovic, M. R., Kumar, S., Morozov, A., Shankar, V., Subramanian, G. & Wilson, H. J. 2022 Understanding viscoelastic flow instabilities: Oldroyd-b and beyond. *Journal of Non-Newtonian Fluid Mechanics* **302**, 104742.

Schnapp, R. & Steinberg, V. 2021 Elastic waves above elastically driven instabiity in weakly perturbed channel flow. *arXiv:2106.01817* .

Shaqfeh, E. S. G. 1996 Purely Elastic Instabilities in Viscometric Flows. *Annual Review of Fluid Mechanics* **28**, 129–185.

Shekar, Ashwin, MucMullen, Ryan M., McKeon, B. J. & Graham, M. D. 2020 Self-sustained elastoinertial Tolmien-Schlichting waves. *Journal of Fluid Mechanics* **897**, A3.

Shekar, Ashwin, MucMullen, Ryan M., Wang, S. N., McKeon, B. J. & Graham, M. D. 2018 Critical-layer structures and mechanisms in elastoinertial turbulence. *Physical Review Letters* **122**, 124503.

Sid, S., Terrapon, V. E. & Dubief, Y. 2018 Two-dimensional dynamics of elasto-inertial turbulence and its role in polymer drag reduction. *Physical Review Fluids* **3**, 01130(R).

Steinberg, Victor 2021 Elastic turbulence: an experimental view on inertialess random flow. *Annual Review of Fluid Mechanics* **53**, 27.

Stuart, J. T. 1960 On the non-linear mechanics of wave disturbances in stable and unstable parallel flows. Part 1. The basic behaviour in plane Poiseuille flow. *Journal of Fluid Mechanics* **9**, 353–370.

Tabor, M. & de Gennes, P. G. 1986 A cascade theory of drag reduction. *Europhysics Letters* **2** (7), 519–522.

Terrapon, V., Dubief, Yves & Soria, Julio 2015 On the role of pressure in elasto-inertial turbulence. *Journal of Turbulence* **16**, 26–43.

Toms, B. A. 1948 Observation on the flow of linear polymer solutions through straight tubes at large Reynolds numbers. *First Intern. Congr. on Rheology* **11**, 135–141.

Vashney, A. & Steinberg, V. 2018 Drag enhancement and drag reduction in viscoelastic flow. *Physical Review Fluids* **3**, 103302.

Virk, P. S. 1970 Drag reduction fundamentals. *AIChE Journal* **21**, 625–656.

Wan, D., Sun, G. & Zhang, M. 2021 Subcritical and supercritical bifurcations in axisymmetric viscoelastic pipe flows. *Journal of Fluid Mechanics* **929**, A16.

Watson, J. 1960 On the non-linear mechanics of wave disturbances in stable and unstable parallel flows. Part 2. The development of a solution for plane Poiseuille flow and for plane Couette flow. *Journal of Fluid Mechanics* **9**, 372–389.

White, C. M. & Mungal, M. G. 2008 Mechanics and prediction of turbulent drag reduction with polymer additives. *Annual Review of Fluid Mechanics* **40**, 235–256.

Xi, L. & Graham, M. D. 2010 Turbulent drag reduction and multistage transitions in viscoelastic minimal flow units. *Journal of Fluid Mechanics* **647**, 421–452.

Xi, L. & Graham, M. D. 2012 Intermittent dynamics of turbulence hibernation in Newtonian and viscoelastic minimal channel flows. *Journal of Fluid Mechanics* **693**, 433–472.

Zhang, Mengqi 2021 Energy growth in subcritical viscoelastic pipe flows. *Journal of Non-Newtonian Fluid Mechanics* **294**, 104581.

Zhang, M., Lashgari, I., Zaki, T. A. & Brandt, L. 2013 Linear stability analysis of channel flow of viscoelastic Oldroyd-B and FENE-P fluids. *Journal of Fluid Mechanics* **737**, 249–279.